Chemical Engineering Journal xxx (xxxx) xxx

Contents lists available at ScienceDirect

Chemical Engineering Journal

journal homepage: www.elsevier.com/locate/cej

Hydrothermal synthesis of novel two-dimensional α-quartz nanoplates and their applications in energy-saving, high-efficiency, microalgal biorefineries

Gyuseop Moon [a,1], Nakyeong Lee [a,b,1], Sungsu Kang [c,d], Jungwon Park [c,d], Young-Eun Kim [a], Sang-Ah Lee [e], Ramesh Kumar Chitumalla [f], Joonkyung Jang [f], Youngson Choe [a], You-Kwan Oh [a,*], Sungwook Chung [a,*]

[a] School of Chemical and Biomolecular Engineering, Pusan National University, 2 Busandaehak-ro 63beon-gil, Geumjeong-gu, Busan 46241, Republic of Korea
[b] Institute for Environment & Energy, Pusan National University, 2 Busandaehak-ro 63beon-gil, Geumjeong-gu, Busan 46241, Republic of Korea
[c] School of Chemical and Biological Engineering, and Institute of Chemical Process, Seoul National University, 1 Gwanak-ro, Gwanak-gu, Seoul 08826, Republic of Korea
[d] Institute for Basic Science (IBS) Center for Nanoparticle Research, Seoul National University, 1 Gwanak-ro, Gwanak-gu, Seoul 08826, Republic of Korea
[e] Department of Environmental Biotechnology, KRIBB School of Biotechnology, University of Science and Technology, Daejeon 34113, Republic of Korea
[f] Department of Nanoenergy Engineering, Pusan National University, 2 Busandaehak-ro 63beon-gil, Geumjeong-gu, Busan 46241, Republic of Korea

ARTICLE INFO

Keywords:
α-Quartz
Nanoplates
Hydrothermal
Microalgae
Biorefinery

ABSTRACT

A facile template-free hydrothermal method was successfully developed for the controlled synthesis of ultrathin α-quartz nanoplates (NPLs) for the first time. Analyses of the α-quartz NPLs revealed the characteristic anisotropic nanostructures of highly crystalline α-quartz with an average lateral size and thickness of 1.14 ± 0.32 μm and 7.7 ± 0.6 nm, respectively. Importantly, efficient extraction of highly valuable chemicals such as astaxanthin (ATX) from the microalgal cells of *Haematococcus pluvialis* (*H. pluvialis*) was accomplished by lacerating the cell walls using the ultrathin α-quartz NPLs under mild ultrasonication. The incorporation of α-quartz NPLs enhanced the ATX extraction efficiency significantly (99%, 18.0 ± 0.6 mg ATX/g cell) when coupled with 5 min of ultrasonication. The dosage of α-quartz NPLs (800.0 mg/L) for maximum ATX extraction was reduced substantially to only 8% of the nanomaterial dose used in the extraction controls. The enhanced extraction efficiency and dosage were explained by the role of the structural anisotropy of α-quartz NPLs in multiple phase separation-extraction processes. This work provides a novel, facile, and economical route for the synthesis of uniform ultrathin nanoplates, offering a new material for the highly efficient harvesting of chemical products from various microalgal biorefinery processes.

1. Introduction

Silicon dioxide (SiO_2 or silica) comprises the two most abundant elements in the Earth's crust, silicon and oxygen. Silica is found in nature and various living organisms. Crystalline silica is an extremely common mineral that exists in at least eight different forms or polymorphs. Quartz is the most abundant polymorph because it is the most thermodynamically stable under ambient conditions. Quartz is present in rocks, soils, and sands and forms from molten magma at ~800 °C and underground hydrothermal veins at temperatures from 250 to 450 °C [1]. Quartz occurs primarily as one of two polymorphs; α-quartz or β-quartz. Both polymorphs have structures based on the helical arrangement of the tetrahedral silicate (SiO_4) unit with the ridgepole of one tetrahedron connected to the keel of the next tetrahedron in a spiral conformation [2]. β-quartz exhibits hexagonal symmetry with 6- and 3-fold screw rotation axes. Structurally, α-quartz is a distorted version of β-quartz and is generally stable at ambient temperature and atmospheric pressure. In contrast, β-quartz is stable only at temperatures above ~573 °C and converts readily to α-quartz upon cooling [3].

Obtaining quartz crystals under ambient conditions is difficult because nucleating quartz normally requires harsh conditions such as high temperatures (300 ~400 °C) and pressures (15 – 100 bar) [4–6].

* Corresponding authors.
E-mail addresses: youkwan@pusan.ac.kr (Y.-K. Oh), sungwook.chung@pusan.ac.kr (S. Chung).
[1] These authors contributed equally to this work.

https://doi.org/10.1016/j.cej.2020.127467
Received 4 August 2020; Received in revised form 15 October 2020; Accepted 19 October 2020
Available online 27 October 2020

Biogenic and biomimetic routes have been used to produce both amorphous and crystalline silica, including cristobalite, tridymite, and quartz [7–11]. Examples include natural biosilification processes exploited by living organisms, such as cyanobacteria [12], diatoms [13], radiolarians [14], and sponges [15] to produce complex and hierarchical silica-based nanostructured frameworks for their skeletons under mild physiological conditions [16–19]. On the other hand, the nucleation and growth processes of the natural biosilification under ambient conditions occur over geologic time. Most of the biosilification products are composed of amorphous silica.

Many synthetic techniques, such as flame, microemulsion, sol–gel, and hydrothermal methods, have been developed to produce novel silica nanostructures because of their unique properties, such as large surface area, excellent chemical, thermal, and mechanical stability [20–22]. Quartz has been produced by precipitation from saturated aqueous silica solutions under hydrothermal conditions for half a century [23,24]. One of the main characteristics of hydrothermal processes is that the temperature of the reaction solvent can be reached near its critical point by heating concurrently with autogenous pressure, making the processes amenable to grow highly crystalline nanomaterials with tunable dimensions in large quantities at relatively low costs [25–28]. There are examples of synthesizing α-quartz nanocrystals with sizes typically ranging from hundreds of micrometers to tens of nanometers. Bertone et al. first developed the synthesis of sub-μm diameter quartz nanocrystals using soluble silica precursors under hydrothermal conditions: temperature above ~250 °C and autogenic pressures within ~5 h [29]. Nevertheless, control of the nanocrystal size, shape, and crystal structure was not superb because of the extremely fast growth rates at these temperatures and the high pH required for the nucleation and rapid coarsening of nanocrystals by Ostwald ripening under basic hydrothermal conditions [29,30]. To overcome these issues, Jiang et al. used an amorphous to crystalline silica transformation to produce single-crystalline α-quartz nanoparticles with a uniform sub-100 nm diameter from Stöber silica nanoparticles and mineralizer additives, such as sodium chloride (NaCl) and sodium hydroxide (NaOH) under hydrothermal conditions of at ~200 °C and ~15 atm within ~3 days [30]. They reported that Stöber silica nanoparticles could be used as templates of uniform sizes that transform to quartz directly by devitrification and minimizing the formation of extra nuclei and aggregation at high pH and NaCl concentrations. Nevertheless, tuning the size and shape of α-quartz nanoparticles was limited by the approximately equiaxed size and shape of the Stöber nanoparticle precursors. Sochalski-Kolbus et al. prepared single-crystalline faceted α-quartz nanorods, ~100 nm × ~10 nm in size, by a microemulsion reaction under solvothermal conditions (~300 °C and < ~100 bar) within the time frame of ~14 – 17 h [31]. Although their techniques generated anisotropic quartz nanorods via fluoride additives that likely controlled the growth of specific facets as a template, they did not exhibit a high degree of control (±10%) of the size and uniformity of the nanorods. Recently, Buckley et al. showed that 1 – 5 nm diameter α-quartz nanocrystals can be initially nucleated from water-oil microemulsions under ambient conditions within ~2 days and then grown to a few tens of nm in size under hydrothermal conditions (~175 °C and ~9 bar) within ~7 days [32]. In terms of the two-dimensional (2D) architecture, 2D silica films composed of epitaxially grown ultrathin SiO_2 layers were fabricated on solid substrates using various growth methods [33]. In addition, 2D mesoporous silica nanoplates and nanosheets with tunable sizes and thicknesses were also prepared in solutions using hard and soft sacrificial templates composed of graphene oxide [34,35], peptides [36,37], diblock copolymers [38], and lamellar micelles [39,40]. Their structures consisted mainly of complex amorphous silica networks with structural defects potentially available for introducing dopants or intercalating small molecular species. On the other hand, the synthesis of highly crystalline silica nanostructures with an anisotropic plate-like morphology has not been reported.

Microalgae are being exploited as the sustainable feedstock of valuable chemicals and have attracted considerable attention in the pharmaceutical, nutraceutical, aquaculture, and biofuel industries [41–46]. Microalgal biorefineries harvest bioactive proteins, carbohydrates, lipids, pigments, and other diverse metabolites produced by microalgae [47]. The processes involved multiple stages, such as cultivation, harvesting, and product extraction and recovery, of which process economics depend on the time and cost constraints for commercial-scale production [48,49]. In particular, cell disruption and intracellular product extraction are considered major technical bottlenecks that are probably due to the robustness and complexity of microalgal cell walls [50]. Various mechanical methods, solely or in combination, such as bead milling, high-pressure homogenization, steam explosion, hydrodynamic cavitation, pulsed electric field, and ultrasonic and microwave agitation have been reported to be capable of disassembling structurally robust microalgal cell walls [50,51]. Mechanical methods have been favored over chemical and biological alternatives for industrial-scale biorefinery operations because of their relatively high efficiency, scalability, and cost-effectiveness, but they are energy-intensive processes. Their mainstream conditions impose thermal and chemical stresses on microalgal cells that degrade the quantity and quality of the bioactive algal products [51,52]. Moreover, their processes usually require relatively long operation times and precise temperature control. Therefore, energy-efficient, sustainable approaches for cell disruption and the extraction of highly valuable algal products under physiologically compatible, stressless conditions are required for efficient large-scale biorefinery applications. One of the promising routes towards these approaches is to apply nanotechnology to the biorefinery of microalgae. Nanomaterials have been exploited to improve the overall processes of microalgal biorefineries, including cell/biomass growth, production of intracellular bioactive compounds, and efficient cell disruption and extraction [53,54]. Nanoparticles composed of silver metal [55], nickel oxide [56,57], organic-aminoclays [58], mesoporous silica [59,60], and carbon nanodots [61] were engineered to harvest intracellular lipid compounds from various algal cells. A recent example using 3 – 5 nm diameter carbon nanodots to extract astaxanthin from lyophilized *Haematococcus pluvialis* (*H. pluvialis*) with a robust, trilayered cell wall resulted in improved extraction efficiency (~85%), nanomaterial dosage (~10 g/L), and extraction time (~6h) [61]. Despite the notable achievements in nanomaterial applications for microalgae biorefinery, a clear picture of the enhancement mechanism has remained elusive in part because of a lack of systematic approaches to understanding the role of the nanomaterial in highly efficient cell wall disruption and extraction.

This paper describes the template-free synthesis of two-dimensional ultrathin α-quartz nanoplates (NPLs) from aqueous dissolution of silica nanoparticles within four hours under facile hydrothermal conditions. To the best of the authors' knowledge, this is the first report on the hydrothermal synthesis of plate- or sheet-like α-quartz nanostructures. A silica precursor solution was prepared by pretreating 60 nm diameter amorphous silica nanoparticles (ASNs) with an aqueous sodium hydroxide (NaOH) solution. The precursor solution was used as a seed in the hydrothermal synthesis of α-quartz NPLs at moderate temperatures and autogenic pressures such as ~250 °C and ~2 – 3 atm. These hydrothermal methods took only a few hours rather than tens of hours to days to complete the synthesis. The α-quartz NPLs obtained had a mean lateral size (LS) and thickness (TN) of 1.14 ± 0.32 μm and 7.7 ± 0.6 nm, respectively. The as-synthesized NPLs had a highly crystalline phase of α-quartz, exhibiting excellent thermal and pH stability under acidic or basic conditions. These α-quartz NPLs were used to extract astaxanthin (ATX; a high-value red antioxidant pigment) from *H. pluvialis*, which is a representative commercial green microalga with a robust, trilayered cell wall. An ATX extraction efficiency of ~99% (18.0 ± 0.6 mg ATX/g cell) was achieved from mild ultrasonication of an α-quartz NPLs and *H. pluvialis* mixture for < 5 min followed by multiple phase separation-extraction processes with minimal cell damage. The α-quartz NPL dosage, i.e. the amount of α-quartz NPL required to achieve the

maximum ATX extraction, was determined to be 800.0 mg/L, which was considerably less than an excess of 10 g/L carbon nanodots necessary for disrupting the cell wall of *H. pluvialis* and extracting an equivalent amount of ATX [61]. The enhancement effects of α-quartz NPL on the recovery of ATX from *H. pluvialis* were rationalized by the characteristic anisotropic structure of α-quartz NPL that facilitated the laceration of the cell wall.

2. Experimental Section

2.1. Materials

Tetramethyl orthosilicate (TMOS, ≥99% Aldrich) and tetraethyl orthosilicate (TEOS, ≥99% Aldrich) were purchased and used as received. All other chemicals including methanol, absolute ethanol, acetone, ammonium hydroxide aqueous solution (NH_4OH, 25 wt%, Daejung), 1 N sodium hydroxide solution (NaOH, Samchun), and 1 N hydrochloric acid solution (HCl, Samchun) were of analytical ACS Regent grade and used as received.

2.2. Preparation of α-quartz NPLs

Stöber et al. reported the synthesis of ASNs via a base-catalyzed hydrolysis and condensation of TEOS [62], and a modified version of this method was used to synthesize monodisperse ASNs, which were then used as precursors for synthesizing α-quartz NPLs [63]. First, 0.225 g of 60 nm diameter ASNs and 3 mL of 1 N NaOH solution were added to 27 mL of triply deionized water and stirred vigorously at 400 rpm for one hour at 100 °C. The solution (pH ≥ 12) changed from a whitish turbid to a clear liquid after ~20 min, which was due likely to the dissolution of ASNs. After stirring for 1 h, ~1 mL of a 1 N hydrochloric acid (HCl) solution was added to neutralize the solution partially, which retained a pH of ≥ 12. The resulting clear suspension was likely composed of silicic precursor ions formed by the complete dissolution of ASNs. The solution was then was transferred to a 100 mL polyether ether ketone (PEEK)-lined stainless-steel autoclave and heated at 250 °C under autogenic pressure with magnetic stirring at under 800 rpm for four hours. Once the reaction was complete, the autoclave was cooled immediately to room temperature. The solution was then filtered through a 0.2 μm nylon membrane, washed with an excess of absolute ethanol and triply deionized water, and dried in a vacuum oven at room temperature to provide ~30 mg of α-quartz NPLs as a white powder.

2.3. Scanning electron microscopy (SEM), transmission electron microscopy (TEM), and X-ray powder diffraction (XRD)

A drop of α-quartz NPL solution diluted in absolute ethanol was placed onto a silicon wafer (4Science Co, Korea) or a holy carbon Quantafoil® TEM grid (Ted Pella, Inc., USA), which had been previously undergone a hydrophilic surface treatment by glow discharge, and dried under vacuum overnight for field emission scanning electron microscopy (FESEM) or transmission electron microscopy (TEM) observations, respectively. The sizes and morphologies of the α-quartz NPLs were investigated by FESEM (Supra 40, Zeiss International, Germany) operated at an accelerating voltage ranging from 5 to 10 kV and by TEM (Hitachi H-7600, Hitachi High-tech, Germany) operated at an accelerating voltage of 80 kV. High-resolution TEM (HRTEM) and selected area electron diffraction (SAED) (TALOS F200X, FEI & Thermo Fisher Scientific Electron Microscopy Solutions, USA) analyses were performed at an acceleration voltage of 200 kV. Aberration-corrected HRTEM imaging (ARM-200F, JEOL Ltd., Japan) was performed at the National Center for Inter-University Research Facilities (Seoul, Korea). The ARM-200F HRTEM microscope was equipped with an aberration corrector in the objective lens and an OneView camera (Gatan, Inc., USA). To minimize the electron-beam-induced amorphization of α-quartz NPLs, it was operated at an acceleration voltage of 60 kV with an electron dose of < ~5 $e^-/Å^2$ to acquire each HRTEM image. The atomistic models of α-quartz NPL were obtained using Visualization of Electronic and STructural Analysis (VESTA) software. The chemical composition of α-quartz NPLs was analyzed simultaneously using an energy-dispersive X-ray spectroscopy (EDS) detector attached to a Supra 40 FESEM (Zeiss International, Germany). X-ray powder diffraction (XRD, X'Pert-MPD, Philips Inc., USA) of α-quartz NPLs was performed using monochromatic Cu $K_{\alpha 1}$ radiation ($\lambda = 0.15405$ nm) operated at 1.2 kW power (40 kV, 30 mA). Custom XRD simulations were conducted using a supercell composed of layered α-quartz nanoplates of 1, 8.6, or 15 nm in thickness, between a vacuum slab with a 0.1 – 1 nm spacing using VESTA software [64].

2.4. Fourier transform infrared (FT-IR) and Raman spectroscopy

Fourier transformation infrared spectroscopy (FT-IR, Spectrum GX, Perkin Elmer Inc., USA) of α-quartz NPLs and ASNs was performed using KBr pellet and attenuated total refection (ATR) techniques. Raman spectroscopy (Nanofinder 30, Tokyo Instrument Inc.) of α-quartz NPLs and ASNs was performed on a micro-Raman spectrometer system using a laser excitation wavelength of 532 nm and reduced laser power (~7 mW) to avoid heating effects under a focused laser beam at the Korea Basic Science Institute (KBSI, Jeonju Center, Korea). Each Raman peak was scanned 20 times using an 1800 G/mm grating at a spectral resolution of 0.92-cm^{-1}/pixel. The measured Raman shifts provided are the means of these measurements, and the errors are reported as ± two standard deviations of the mean.

2.5. Thermogravimetric analysis (TGA)

Thermal analyses of α-quartz NPLs and ASNs were carried out using a thermal gravimetric analysis/differential thermal analysis (TGA/DTA) analyzer (SDT Q600, TA Instrument Inc., USA). Typically a ~10 mg sample was heated in an Al_2O_3 crucible at a heating rate of 5 °C/min under an N_2 gas flow rate of 100 mL/min up to 750 °C.

2.6. ^{29}Si solid-state nuclear magnetic resonance (ssNMR) spectroscopy

^{29}Si solid-state nuclear magnetic resonance (ssNMR) spectroscopy (400 MHz AVANCE III HD, Bruker Corporation) of α-quartz NPLs and ASNs was performed using a 4 mm (outer diameter of a zirconia rotor) magic angle spinning (MAS) probe at the Korea Basic Science Institute (KBSI, Western Seoul Center, Korea). The spectra were obtained using direct excitation at 79.51 MHz with a 1.6 μs pulse width (pulse angle π/6), a 50 s recycle delay at ambient probe temperature (~25 °C), and a sample spin rate of 11 kHz. The signals from 4900 scans were accumulated. The ^{29}Si NMR chemical shifts (δ in ppm) were referenced to an external sample of tetrakis(trimethylsilyl) silane at −135.5 ppm with respect to tetramethylsilane (TMS) at 0.0 ppm.

2.7. X-ray photoelectron spectroscopy (XPS)

XPS (ESCALAB 250, Thermo Fisher Scientific Inc., USA) of α-quartz NPLs and ASNs was performed using a monochromatic X-ray excitation source of Al anode K_α radiation (1486.6 eV). The binding energies were calibrated versus the C 1 s line of carbon at 284.6 eV before the actual measurements.

2.8. Nitrogen (N_2) physisorption experiments for Brunauer-Emmett-Teller (BET) and Barrett-Joyner-Halenda (BJH) analysis

N_2 adsorption–desorption measurements of α-quartz NPLs and ASNs were performed using an Autosorb-iQ surface area and pore size analyzer (Quantachrome Instruments, USA). Samples of α-quartz NPLs and ASNs were degassed at 300 °C for ~3 h before the measurements. The BET method was used to calculate the specific surface areas. The

pore size distributions of α-quartz NPLs and ASNs were calculated from the desorption branches of their isotherms using the BJH method.

2.9. Culture conditions of microalga H. pluvialis cells

The *H. pluvialis* NIES-144 cyst cells used in this study were obtained from the National Institute for Environmental Studies (NIES), University of Tokyo, Japan. The NIES-C medium [45,49] was used for the photoautotrophic cultivation of this strain and contained the following (per liter): 0.15 g $Ca(NO_3)_2$, 0.10 g KNO_3, 0.50 g tris(hydroxymethyl)aminomethane (Tris), 0.05 g β-glycerophosphoric acid disodium salt pentahydrate, 0.04 g $MgSO_4{\cdot}7H_2O$, 0.01 mg thiamine, 0.10 μg biotin, 0.10 μg vitamin B_{12}, and 3.00 mL PIV metal solution. One liter of PIV metal solution consisted of 1.0 g Na_2EDTA, 0.196 g $FeCl_3{\cdot}6H_2O$, 36.0 mg $MnCl_2{\cdot}4H_2O$, 22.0 mg $ZnSO_4{\cdot}7H_2O$, 4.0 mg $CoCl_2{\cdot}6H_2O$, and 2.5 mg $Na_2MoO_4{\cdot}2H_2O$. After adjusting its pH to 7.5, the NIES-C medium was sterilized by filtration through a 0.2 μm membrane. One colony of *H. pluvialis* from an agar-plate culture was transferred to a 250-mL Erlenmeyer flask with a porous silicon stopper (working volume, 100 mL). The flask was then incubated for 90 days in a shaking incubator (GC-300, JEIO TECH, Korea; 150 rpm and 25 °C) under continuous illumination at 90 μmol/m^2/s. The light intensities and pH values were measured simultaneously using a quantum photometer (LI-250Am Li-Cor Inc., USA) and a pH meter (HM-30R, TOADKK, Japan), respectively. Detailed of the culture conditions are reported elsewhere [45,61]. For the α-quartz NPL extraction experiments, mature *H. pluvialis* cyst cells (obtained by cultivation for 90 days) were harvested by centrifugation at 4,000 rpm for 10 min (Combi-514R, Hanil Science Inc., Korea) and freeze-dried for three days (FD5512, IlShin BioBase Co., Korea). The lyophilized cyst cells were preserved in a vacuum bag at −20 °C until further use.

2.10. Determination of the total astaxanthin (ATX) content from H. pluvialis

The total ATX contents of lyophilized *H. pluvialis* cyst cells were determined by bead-beater assisted solvent extraction and high-performance liquid chromatography (HPLC; Agilent 1260 infinity, Hewlett Packard, USA). Briefly, 1 mL of dichloromethane/methanol (DCM/MeOH; 1:1, v/v) containing 0.025 N NaOH and 1.0 g glass beads (1.5 mm diameter, Daihan Scientific, Korea) were added to ~10 mg of cyst cells in a 1.5 mL bead beating tube, and then vigorously homogenized using a FastPrep-24™ bead beater (MP Biomedicals, USA; 6 m/s for 30 s and three times). After centrifugation at 10,000 rpm for 3 min (Sorvall Legend Micro 17R, Thermo Fisher Scientific, USA), the ATX-containing solvent layer was collected in a new tube and kept at 4 °C for two hours in the dark to allow saponification. Bead-beater assisted solvent extraction was repeated three more times until all of the red-colored cyst cells were colorless. The ATX extracts were filtered through a 0.2 μm polytetrafluoroethylene (PTFE) membrane filter and analyzed by HPLC, as described previously [61]. The mean ATX content of the *H. pluvialis* cyst cells was determined to be 18.2 ± 0.6 mg/g cell. HPLC analysis was used to identify the other ketocarotenoid pigments without the saponification reaction. The carotenoid reference standards astaxanthin, canthaxanthin, lutein, neoxanthin, and zeaxanthin were used as supplied (Sigma Aldrich, USA).

2.11. Cell disruption and α-quartz NPL assisted ATX extraction from H. pluvialis

An algal solution of 800 mg cell/L, which was considered to be typical for *H. pluvialis* cell concentrations, was prepared using freeze-dried *H. pluvialis* and purified Milli-Q® water under ambient conditions [65]. This solution was then mixed vigorously (Vortex 3, IKA, Germany), and 5 mL aliquots were dispensed into 12 mL Pyrex-glass tubes with a Teflon-sealed screw stopper. α-Quartz NPLs (a white powder) was added to tubes to concentrations of 100 – 800 mg/L and briefly vortexed briefly for 2 – 3 s. The resulting solutions were then treated for 5 min in an ultrasonic bath (2510-DTH, Branson, USA; 40 kHz, 100 W) to provide sufficient physical contact between the α-quartz NPLs and algal cells during ultrasonication. Instead of using the ultrasonic agitator, FastPrep-24™ bead beater equipment was used for ATX extraction. On the other hand, the ATX extraction efficiency was very low at 3.4 ± 0.3%. Therefore, no further experiments were conducted using the FastPrep-24™ bead beater. The α-quartz NPLs-treated cells were collected by centrifugation at 3,000 rpm for 5 min (Combi-514R, Hanil Science Inc., Korea) for the subsequent solvent extraction of intracellular ATX. Five milliliters of a solution of the anhydrous DCM/MeOH mixture (1:1, v/v) was added to the tubes containing α-quartz NPL treated cells, vortexed once briefly, and kept at ambient temperature for 30 min. The resulting solutions were transferred to new 12 mL Pyrex-glass tubes, centrifuged at 3,000 rpm for 5 min, and evaporated with N_2 gas (99.9% purity) at 25 °C using an N-EVAP evaporator (Organomation Associates Inc., USA). The amounts of ATX extracted from *H. pluvialis* were analyzed by HPLC. The ATX extraction efficiencies (calculated as the percentages of the total ATX contents of cells before the α-quartz NPL treatment) were measured as a function of the ultrasonication and extraction times (30–120 min and 0.5–24 hr, respectively). As controls, freeze-dried *H. pluvialis* cyst cells were sonicated for 5 min in the absence of the α-quartz NPLs or with conventional 180 nm diameter spherical ASNs at 100 – 800 mg/L. The ATX extraction efficiencies were also measured as a function of the ultrasonication and extraction time of 5 and 30 min, respectively.

2.12. α-Quartz NPLs assisted ATX recovery by multiple phase separation-extraction processes

An algal solution of 800 mg cell/L was prepared using freeze-dried *H. pluvialis* and purified Milli-Q® water. This solution was mixed vigorously (Vortex 3, IKA, Germany) and dispensed in 5 mL aliquots into 12 mL Pyrex-glass tubes with a Teflon-sealed screw stopper. The α-quartz NPLs were added to tubes to a concentration of 800 mg/L and briefly vortexed for 2 – 3 s. The solutions were ultrasonicated for 5 min and centrifuged at 3,000 rpm for 5 min to remove the aqueous supernatants. Subsequently, 5 mL of anhydrous DCM/MeOH (1:1, v/v) was added and left for 30 min to extract ATX. After extraction, 5 mL of Milli-Q® water was added to produce a DCM/MeOH/water mixture (0.5:0.5:1, v/v/v). This mixture exhibited aqueous-organic phase separation with a whitish aqueous upper phase and a clear red colored organic lower phase, but anhydrous DCM/MeOH alone did not produce phase separation (see Figs. S12 and S13, Supplementary material). The DCM/MeOH/water was then vortexed vigorously until most of the color has been removed from the organic phase, indicating the almost complete transfer of ATX and α-quartz NPLs into the organic DCM and aqueous MeOH/water phases, respectively. Lower organic phases were separated and the amounts of ATX present were determined by HPLC. The upper aqueous phase was also separated and centrifuged to recover the algal cell/α-quartz NPL precipitate. This phase separation-extraction process involving multiple steps of α-quartz NPL-assisted cell wall disruption, phase separation, ATX extraction, and algal cell-α-quartz NPLs recovery was repeated three times in duplicate. The average values were subjected to analysis, and the measurement errors were < +/- 5%.

2.13. Morphological characterization of H. pluvialis before and after α-quartz NPLs treatment

The morphological features of *H. pluvialis* cyst cells, i.e., color, cell size, and cell wall thickness, were investigated using an Axio Imager.A2 optical microscope equipped with ZEISS ZEN software (Carl Zeiss, Germany) [45]. Detailed surface morphologies before and after the α-quartz NPL treatment were examined by scanning electron microscopy (SEM; FEI Quanta 250 FEG, Thermo Fisher, USA). The samples for SEM

analyses were fixed in a 1.5% paraformaldehyde-glutaraldehyde fixation solution, pasted on a glass plate, air-dried at ambient temperature, set in a sample holder, and coated with platinum at ~8 nm by sputtering for 80 s (Quorum Q150T S, UK).

2.14. Flow cytometry of H. pluvialis before and after α-quartz NPLs treatment

The cell disruption level caused by the NPL treatment was assessed using a flow cytometer (Facscanto II, Becton-Dickinson, USA) equipped with an argon-ion laser (excitation 488 nm, 20 mW power) and fluorescent phycoerythrin (PE) filter. The instrument was set up to measure the linear forward light scatter (FSC: a measure of cell size) and 90° side light scatter (SSC: a measure of cell granularity).

2.15. Zeta-potential measurements of H. pluvialis before and after α-quartz NPLs treatment

The zeta-potentials were measured in triplicate using a Zetasizer equipped with a He-Ne laser at 633 nm (Nano ZS90, Malvern Instruments, UK) at ambient temperatures.

2.16. Statistical data analysis

SPSS Statistics 17.0 software (IBM 173 Co., USA) was used for the data analysis. The experimental results are presented as the means ± standard deviations of three independent experiments. A student's *t*-test was conducted using Microsoft Excel®, and P values<0.05 were considered statistically significant ($^*P < 0.05$).

3. Results and discussion

3.1. FT-IR, ^{29}Si ssNMR, Raman, XPS, and TGA analysis of α-quartz NPLs

The FT-IR spectra of the as-synthesized α-quartz NPLs (Fig. 1A) exhibited several characteristic IR spectral bands. The IR absorption bands at 3437 and 3242 cm^{-1} were assigned to the O–H stretch of surface silanol and adsorbed H_2O [66]. The band at ~1638 cm^{-1} was assigned to the bending vibration of adsorbed H_2O [66]. The main IR bands at 1104, 800, and 474 cm^{-1} were attributed to the asymmetric and symmetric stretch vibrations, and symmetric bending vibrations of the Si-O-Si bonds, respectively [67,68]. Overall, the characteristic IR bands of α-quartz NPLs were similar to those of the 60 nm diameter ASNs used as the starting materials (Fig. 1A) except for a missing band at 946 cm^{-1}, which was attributed to Si-OH bond stretch [69]. Although the

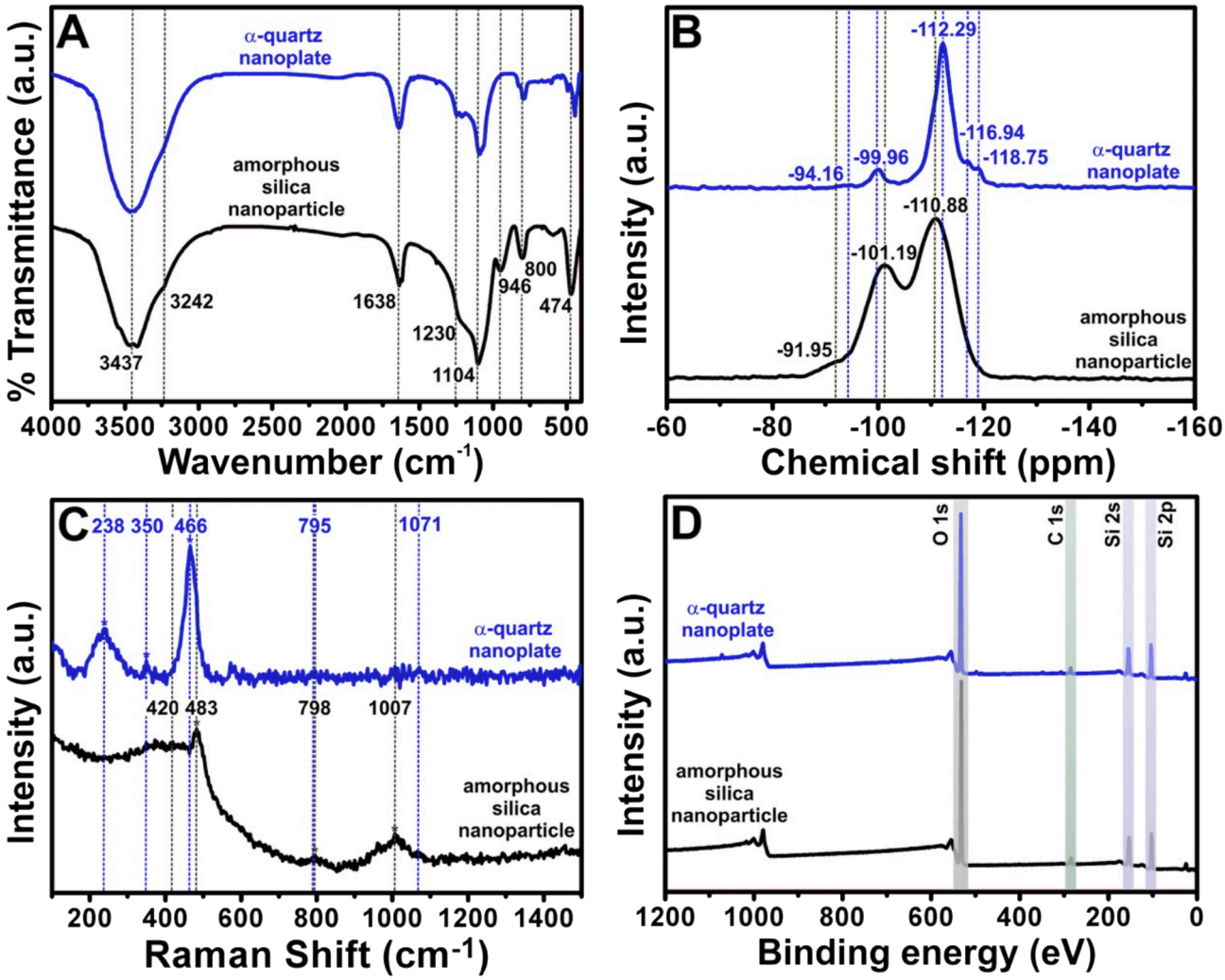

Fig. 1. (A) FT-IR, (B) ^{29}Si ssNMR, (C) Raman, and (D) XPS spectra of α-quartz NPLs (blue) and ASNs (black). (B) ^{29}Si ssNMR and (C) Raman spectroscopy results clearly distinguished the crystalline and amorphous phases, and results were consistent with those obtained by XRD and SAED analysis (Fig. 3). (For interpretation of the references to color in this figure legend, the reader is referred to the web version of this article.)

reasons for the absence of the band at 946 cm^{-1} could not be determined, there may be fewer free hydroxyl groups on the surfaces of α-quartz NPLs than on those of the ASNs.

Fig. 1B shows the ^{29}Si solid-state nuclear magnetic resonance (ssNMR) spectra of α-quartz NPLs and 60 nm diameter ASNs. The spectrum of α-quartz NPLs (blue curve) was dominated by three characteristic peaks at −112.29 (including shoulders at −116.94 and −118.75), −99.96, and −94.16 ppm, which were assigned to non-hydroxy terminated Q^4 ($(-O)_4Si$), monohydroxy terminated Q^3 ($(-O)_3Si(OH)$), and dihydroxy terminated Q^2 ($(-O)_2Si(OH)_2$) sites, respectively. A few aspects of the spectra of α-quartz NPLs and ASNs are worth addressing. First, the spectral width of the α-quartz NPLs was much narrower than that of the 60 nm diameter ASNs (i.e., full width at half maximums (FWHMs) of α-quartz NPL peaks were < 42% of those of ASNs), indicating that variations in Si-O-Si angles from those in crystalline NPLs with ordered silica networks were smaller than those of ASNs with disordered networks (see Fig. S1A, Supplementary material). Second, when the fractions of Q^n sites (n = 2, 3, and 4) in α-quartz NPLs and ASNs were determined from deconvoluted Lorentzian-Gaussian peak areas in the ^{29}Si ssNMR spectra (indicated by multi-color curves in Figs. S1B and S1C, Supplementary material, and summarized in Table S1, Supplementary material). The Q^n values for α-quartz NPLs were 0.9% for Q^2, 7.6% for Q^3, and 91.5% for Q^4 sites, while those of ASNs were 4.6% for Q^2, 37.3% for Q^3, and 58.1% for Q^4 sites. The 60 nm diameter ASNs would have larger Q^3 and Q^2 values than α-quartz NPLs because of their higher surface to volume ratios and smaller sizes. On the other hand, these values compared reasonably well with the 27.5% for Q^3 and 2% for Q^2 of silica nanoparticles [70], and the 35.3% for Q^3 and 4.7% for Q^2 of quartz nanocrystals [32] having many surfaces along, or close to, lower energy {1 0 1} planes via structural reorganizations when their sizes were reduced to the nanometer length scale. The $Q^2 + Q^3$ to Q^4 ratio of α-quartz NPLs was 0.09, which was ~7.8 times smaller than the 0.72 of ASNs (Table S1, Supplementary material). By applying a simple scaling approach based on the geometric structures (Fig. S2, Supplementary material), $Q^2 + Q^3$ to Q^4 ratios of α-quartz NPLs and ASNs, which were proportional to the surface to volume contribution, were estimated based on the assumption that free surface hydroxyl groups were distributed uniformly at both the Q^2 and Q^3 sites. Fig. S3 shows the calculated $Q^2 + Q^3$ to Q^4 ratios as a function of the sizes of ASNs, α-quartz NCs, and α-quartz NPLs on this scaling approach (Supplementary material). The estimated ratios agreed with the ratios obtained from the ^{29}Si ssNMR measurements provided the lateral sizes of NPLs were larger than ASN diameters by 1 – 2 orders of magnitude. This difference in the length scale was consistent with the FESEM, TEM, and atomic force microscopy (AFM) results (Fig. 2). Therefore, the lower ratio of $Q^2 + Q^3$ to Q^4 sites of α-quartz NPLs was attributed to only one length scale of the anisotropic nanoplates reduced in nanometers versus the concurrence of all three nanometer scales of isotropic nanoparticles.

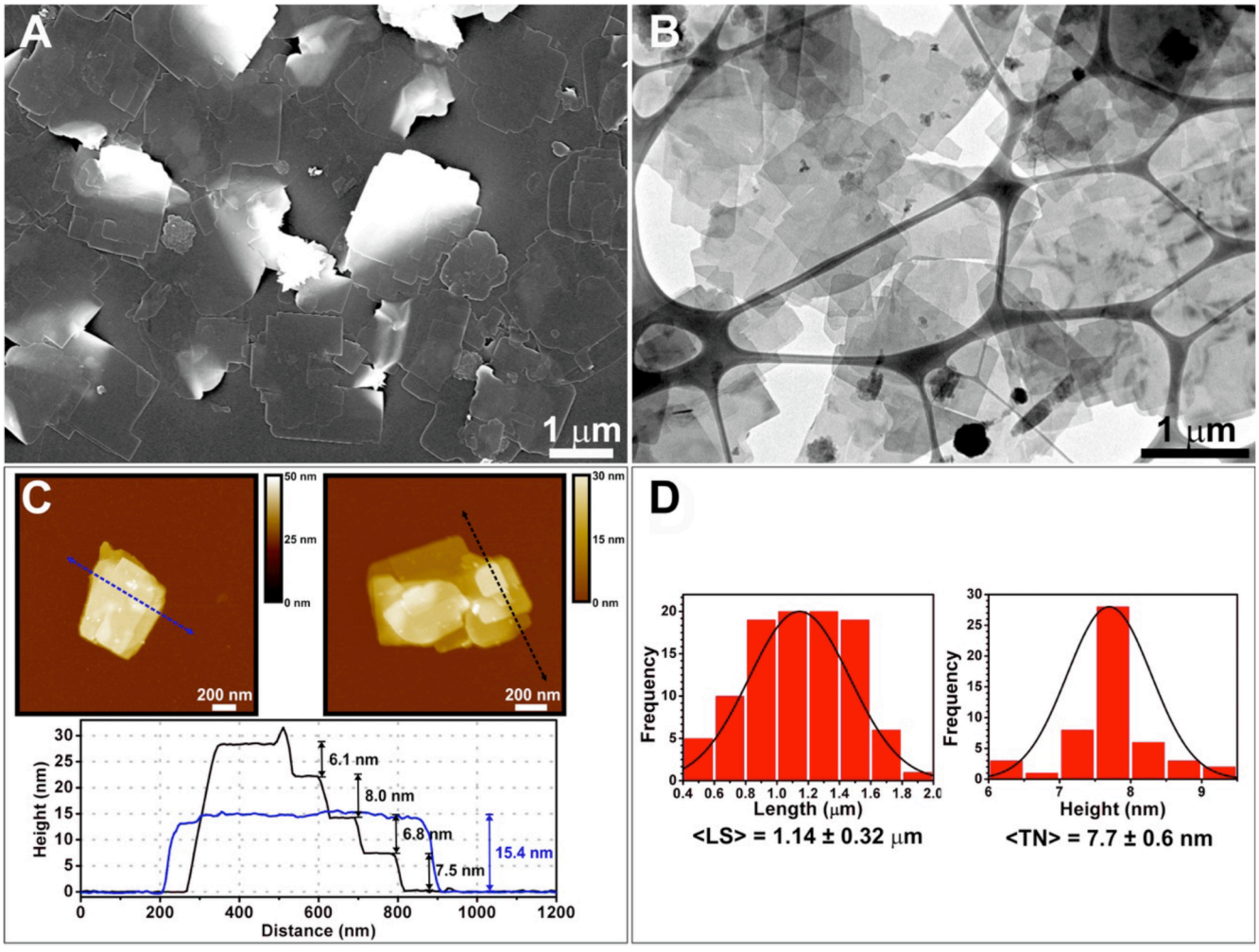

Fig. 2. Representative FESEM (A) and TEM (B) micrographs of as-synthesized α-quartz NPLs. (C) Representative AFM height images of α-quartz nanoplates and their height profiles showing layered α-quartz NPLs. (D) The corresponding distributions of the measured lateral sizes (LS) (mean 1.14 ± 0.32 μm, based on 100 counts) and thicknesses (TN) (mean 7.7 ± 0.6 nm, based on 50 counts) of α-quartz NPLs. (For interpretation of the references to color in this figure legend, the reader is referred to the web version of this article.)

In addition, this decrease in ratio suggested that α-quartz NPLs had fewer free surface hydroxyl groups than ASNs, which is also consistent with the observed absence of the characteristic IR band (946 cm^{-1}) due to the surface hydroxyl groups for α-quartz NPLs.

Fig. 1C shows the Raman spectra of the as-synthesized α-quartz NPLs (blue curve) and ASNs (black curve). Bulk crystalline α-quartz has two enantiomorphs with the space group $P3_121$ (D_3^5) (right-handed) and $P3_221$ (D_3^6) (left-handed). The irreducible representation of the optical vibration for the D_3 group may be expressed as $\Gamma_{irr} = 4A_1 + 4A_2 + 8E$, where the A_1 modes are Raman-active, A_2 modes are IR-active, and the E modes are both Raman- and IR-active. The A_2 and degenerate E modes are split by long-range Coulomb forces into longitudinal and transverse optical (LO and TO) components [71]. Bulk α-quartz has characteristic Raman modes at 128 (strong), 207 (strong), 265 (medium), 356 (very weak), 394 (very weak), 464 (very strong), 795 (very weak), and 1085 cm^{-1} (very weak), which are due to vibrations based on the assigned symmetries of $E(LO + TO)$, A_1, $E(LO + TO)$, A_1, $E(TO)$, A_1, $E(TO)$, $E(TO)$, and A_1, respectively [71,72]. The principal Raman modes of as-synthesized α-quartz NPLs observed at 238 and 466 cm^{-1} in Fig. 1C were attributed to the Raman-active A_1 modes. The other Raman bands from the bulk α-quartz were not detected for α-quartz NPLs. Moreover, the Raman spectrum of the crystalline α-quartz NPLs (blue curve) differed appreciably from that of the ASNs (black curve). The key differences included the overall shape of the spectra, the missing A_1 mode Raman band at 238 cm^{-1} (medium), and the location of the A_1 mode Raman band (i.e., 466 cm^{-1} (strong) vs. 483 cm^{-1} (strong)). These bands were attributed to differences in the degree of crystallinity and structural anisotropy. Overall, Raman spectroscopy provided a better means of differentiating the crystalline and amorphous phases than IR.

Fig. 1D presents the survey XPS spectrum of the as-synthesized α-quartz NPLs. The survey XPS spectra over the full energy range confirmed the existence of common elements such as Si and O and the survey XPS spectrum of as-synthesized α-quartz NPLs resembled that of ASNs. High-resolution XPS scans of the as-synthesized α-quartz NPLs and ASNs (Fig. S4, Supplementary material) provided the following binding energies (BEs): Si 2p peaks at 103.4 and 103.2 eV and O 1 s peaks at 532.6 and 532.4 eV, respectively. Although both peaks of α-quartz NPLs were located at marginally higher BEs than those of ASNs, the BEs were reasonably consistent with the values reported for bulk quartz [73], amorphous silica nanoparticles [63,74,75], and mesoporous silica [76,77].

TGA of the as-synthesized α-quartz NPLs and ASNs (Fig. S5, Supplementary material) showed that α-quartz NPLs had excellent thermal stability, i.e., it showed less than 4% weight loss compared to ASNs over the temperature range from 50 to 800 °C. Although the FT-IR, XPS, and TGA results indicate that the overall chemical environment of α-quartz NPLs is similar to that of ASNs, Raman and ^{29}Si ssNMR spectroscopy differentiated the amorphous and crystalline forms of silica.

3.2. Structural analysis of α-quartz NPLs by FESEM, TEM, and AFM

Fig. 2A, 2B, and 2C present FESEM, TEM, and AFM micrographs of

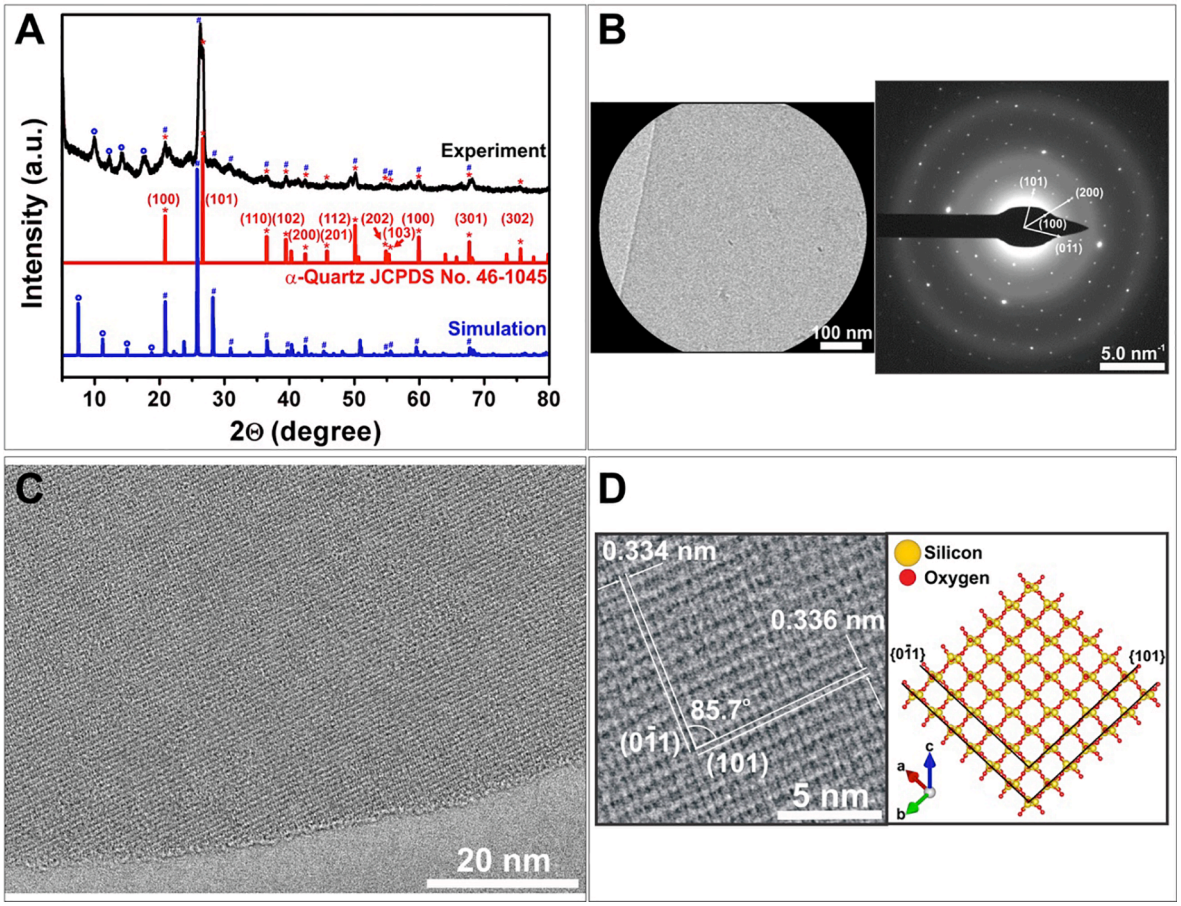

Fig. 3. (A) Powder XRD patterns of the as-synthesized α-quartz NPLs (black curve), bulk α-quartz (red curve), and simulated XRD patterns of layered α-quartz NPLs (blue curve). (B) Bright-field TEM image of a α-quartz NPL selected for diffraction analysis (left) and its corresponding selected area electron diffraction (SAED) pattern (right). (C) Representative HRTEM image of a α-quartz NPL. (D) Higher magnification HRTEM micrograph of single-crystalline α-quartz NPL (left) and its corresponding atomistic model projected along the $[1\bar{1}1]$ direction showing the (101) and $(0\bar{1}1)$ planes of α-quartz running diagonally at a dihedral angle of 85.7°. (For interpretation of the references to color in this figure legend, the reader is referred to the web version of this article.)

the as-prepared α-quartz NPLs with either a plate- or sheet-like morphology with a relatively uniform size distribution. The average lateral size (LS) and thickness (TN) of the α-quartz NPLs samples measured by FESEM, TEM, and AFM were 1.14 ± 0.32 μm and 7.7 ± 0.6 nm, respectively.

The XRD patterns of the α-quartz NPLs demonstrated their crystalline nature (Fig. 3A). Most peaks in the XRD pattern (black curve) were in accordance with that of bulk α-quartz (International Centre for Diffraction Data (ICDD) card no. 00–046-1045 and Joint Committee on Powder Diffraction Standards (JCPDS) card no. 46–1045). Other unassigned peaks were observed at low diffraction angles ($0 < 2\Theta < 20$), and a peak due to the (1 0 1) reflection showed a slight shift in its position. The simulated XRD pattern (blue curve) did not reproduce any peaks in this low 2Θ range except when a vacuum slab was introduced above and below the layer of the α-quartz NPL in a supercell (Experimental Section). Although the positions of low angle peaks were not matched precisely, the best simulated XRD pattern was obtained for a 15 nm thickness of NPL with a 0.1 nm vacuum slab spacing gap. This suggests that α-quartz NPLs were likely stacked and in a powdery state presumably due to hydrophilic surface interactions.

Fig. 3B presents the selected area electron diffraction (SAED) pattern of a typical α-quartz NPL of a single crystal, as indicated by a well-ordered pattern of diffraction spots, which were assigned to the (101), (200), $(\bar{1}01)$, and $\left(0\bar{1}1\right)$ planes based on the *d*-spacings calculated from its SAED pattern (Table 1). These *d*-spacings matched the reflections of bulk α-quartz closely and were in good agreement with the XRD results (Fig. 3A).

The HRTEM micrographs in Fig. 3C and 3D show lattice fringes of the α-quartz NPLs consistent with an almost defect-free, single-crystalline domain with dimension up to a few μm. The interplanar distances of the lattice fringes shown in Fig. 3D were 0.334 and 0.336 nm, which were assigned to those of the $(\bar{1}01)$ and $\left(0\bar{1}1\right)$ planes of α-quartz, respectively. These two planes were running along diagonally with a dihedral angle of 85.7°. These findings agree well with a reported interplanar spacing of 0.334 nm and an angle of 86° for bulk α-quartz crystal, and are consistent with the lattice structure of α-quartz NPL. Fig. 3D shows the atomic arrangement projected along the $\left[\bar{1}11\right]$ zone axis [78,79].

3.3. Microalgae extraction experiment

The effects of the α-quartz NPLs on the extraction and recovery of ATX from *H. pluvialis* cysts cells were investigated by bright-field optical microscopy, FESEM, flow cytometry, HPLC, and using zeta-potential measurements.

Fig. 4 shows the typical cell size and cell wall thickness distributions of *H. pluvialis* cysts as determined by optical microscopy and image analysis. The cell diameter of *H. pluvialis* cysts cell ranged from 17 to 65 μm (average diameter of 31.5 ± 10.4 μm), indicating a heterogeneous cell population under typical culture conditions. Nevertheless, this distribution concurred with that reported for *H. pluvialis* (i.e. average diameter of 34.8 ± 5.6 μm) cultured under a red light using a bubble-column photobioreactor [80]. The average cell wall thickness of the *H. pluvialis* cysts cells was 2.8 ± 1.2 μm, which was comparable to that of the *H. pluvialis* cyst cells cultured for 2 – 3 weeks [81].

Table 1
Summary of the diffraction analysis results and assignments for α-quartz NPLs.

Measured diffraction SAED (1/nm)	Measured d-spacing SAED (1/nm)	Assignment	Measured diffraction XRD (2Θ (intensity))
2.994	0.334	α-Quartz $(\bar{1}01)$ at 0.334 nm	25.8, 26.6(s)
2.974	0.336	α-Quartz $\left(0\bar{1}1\right)$ at 0.334 nm	25.8, 26.6(s)
2.363	0.423	α-Quartz (101) at 0.425 nm	20.8(m)
4.732	0.221	α-Quartz (201) at 0.213 nm	42.5(w)

Fig. 5 presents a set of *in situ* optical microscopy images selected from a time sequence. The images reveal a multi-stage biorefinery process comprised of three distinct stages: (1) mature *H. pluvialis* cysts growth, (2) fractional disruption of cell walls induced by α-quartz NPLs under ultrasonic conditions, and (3) recovery of ATX by the solvent extraction of ATX-containing lipid droplets likely at sites lacerated by α-quartz NPLs. As shown in Fig. 5B, 5C, and 5D, mature *H. pluvialis* cyst cells appeared to be intact under 5 min of ultrasonication (Fig. 5B). Furthermore, even after 30 min extraction with anhydrous dichloromethane (DCM)/methanol (MeOH), the cell shapes, morphologies, and color intensities remained unchanged (Fig. 5C and 5D). In contrast, after adding α-quartz NPLs, the intracellular circular domains containing red-ATX-containing lipids appeared to be slightly smaller, and the intracellular contrast of the region between the outer perimeter of these circular domains and cell walls was altered significantly (Fig. 5B^{+}).

Rugged granular patterns were visible within the region between the outer perimeter of these circular domains and cell walls under typical brightfield illumination or showed in differential interference contrast imaging, probably due to the light scattering effects of α-quartz NPLs. On the other hand, finer details were not observable because of the resolution limit of optical microscopes. These observations indicate that some α-quartz NPLs penetrated and accumulated within cell walls, which is in-line with the FESEM measurements shown in Fig. 6. After introducing the DCM/MeOH, red-ATX-containing lipid droplets began to emerge from the cyst cells (Fig. 5C^{+}). In particular, after an extended extraction period of 30 min, almost all ATX was released by the α-quartz NPL treated cells (Fig. 5D^{+}). In contrast, no ATX was retrieved from the cells not treated with α-quartz NPLs, and the cell structural integrities were preserved (Fig. 5D).

Ex situ FESEM analysis confirmed the presence of α-quartz NPLs either at or in the vicinity of the *H. pluvialis* cysts (Fig. 6; see Experimental Section for details of the procedure). Fig. 6C and 6D show the ATX-containing lipid residues and α-quartz NPLs embedded in the cell walls during extraction, indicating that ATX-containing lipids were likely to have been released from the lesions generated in cell walls by α-quartz NPLs.

Fig. S6 (Supplementary material) shows flow cytometry measurements of *H. pluvialis* cysts before and after treatment with α-quartz NPLs. The relative population P1 identified from the measurements gradually increased by ~10% after 5 min of ultrasonication in the absence of α-quartz NPL but increased by ~23% in their presence, whereas relative population P2 showed a continuous decline, indicating the extent of algal cell disruption. The forward versus side scatter profiles of P1 and P2 treated with α-quartz NPLs showed a slight shift to the left (i.e., to a smaller size) as compared to the cells exposed to ultrasonication alone, indicating a surge of forming smaller cells and cell debris from α-quartz NPLs-assisted algal cell disruption. These observations are consistent with the optical microscopy and FESEM results (Figs. 5 and 6, respectively).

Fig. 7 presents the ATX extraction efficiencies from the 90 day-cultured *H. pluvialis* cyst cells after treatments of α-quartz NPLs. When the cyst cells were ultrasonicated for 5 min without anisotropic α-quartz NPLs or 180 nm diameter isotropic ASNs and then extracted for 30 min with anhydrous DCM/MeOH (1:1, v/v), the ATX extraction efficiencies were 8.6 ± 0.9% and 7.0 ± 0.7%, respectively. Treatment with α-quartz NPLs improved extraction efficiency to 35.4 ± 0.5% significantly. Furthermore, the extraction efficiency of α-quartz NPLs increased gradually with increasing concentration before saturation at an α-quartz NPL concentration of > 800 mg/L (Fig. S8, Supplementary material). These results show that ultrasonication, followed by solvent extraction alone, did not result in effective ATX recovery. Moreover, the α-quartz

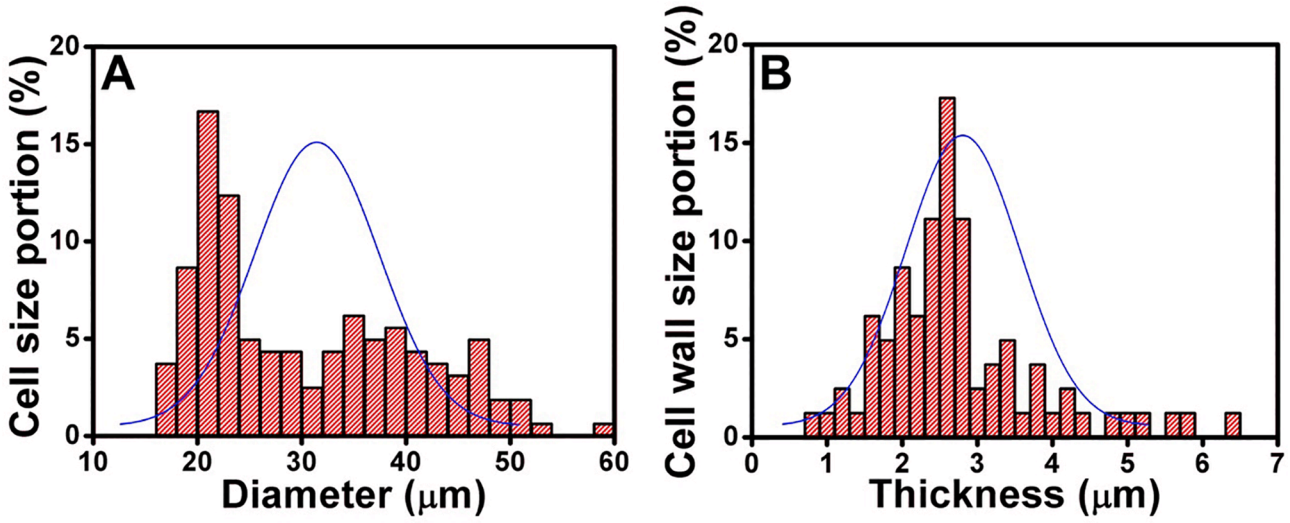

Fig. 4. Distributions of (A) cell size and (B) cell wall thickness of *H. pluvialis* cyst cells cultured for 90 days under photoautotrophic conditions. (For interpretation of the references to color in this figure legend, the reader is referred to the web version of this article.)

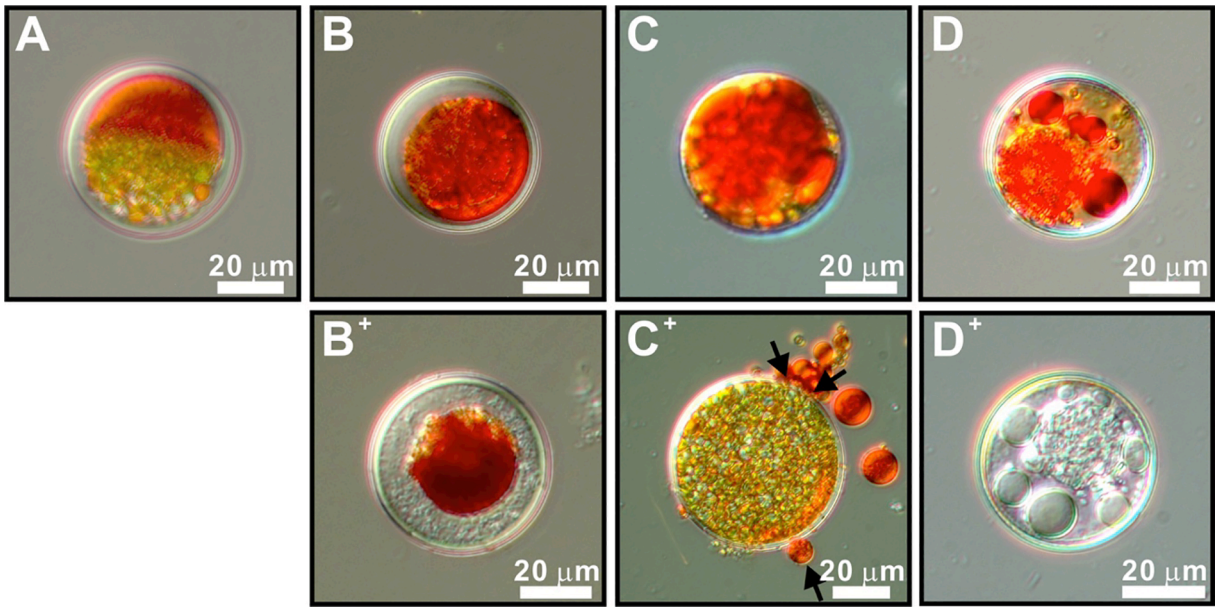

Fig. 5. Series of *in situ* optical microscopy images of cell wall disruption and astaxanthin (ATX) extraction from *H. pluvialis* cyst cells (B – D) processed without or (B^+ – D^+) with α-quartz NPLs. (A) Initial mature cyst. (B and B^+) Intact mature cyst after 5 min of ultrasonication. (C and C^+) and (D and D^+) Mature cyst after subsequent solvent extraction for 30 s and 30 min, respectively. The intracellular contrast difference between (B) and (B^+) near the cell wall implies the presence of α-quartz NPLs inside the cyst. (C) and (C^+) show a mature cyst during the extraction process, and show the extraction of red-ATX-containing lipid droplets only from the cyst treated with α-quartz NPLs. The black arrows in (C^+) and the FESEM image in Fig. 6 suggest that the droplets were released from lacerations generated in the cell walls by α-quartz NPLs. (D) and (D^+) show mature cyst after extraction, and that ATX was fully extracted from the cyst treated with α-quartz NPLs. (For interpretation of the references to color in this figure legend, the reader is referred to the web version of this article.)

NPLs were responsible for the observed efficiency improvement. Furthermore, the structural anisotropy of ultrathin α-quartz NPLs might play a critical role in the laceration of the cell wall.

Multiple solvent extractions are always more efficient than a single extraction, particularly if the algal compound does not have an extremely high partition coefficient in the organic solvent. Fig. S9 (Supplementary material) shows ATX extraction efficiencies after three cycles of α-quartz NPL-assisted cell wall disruption followed by anhydrous DCM/MeOH (1:1, v/v) extraction. The extraction efficiency in the absence and presence of α-quartz NPLs using DCM/MeOH (1:1, v/v) increased marginally from 5.8 ± 0.1% (single extraction) to 26.0 ± 0.5% (triple extraction) and 35.4 ± 2.5% (single extraction) to 58.9 ± 9.5% (triple extraction), respectively. In addition, the extraction efficiency of single ATX extraction with α-quartz NPLs improved from of 35.4 ± 0.5% to 53.9 ± 5.8% when sufficient H_2O was added to cause DCM/MeOH-H_2O (1:1 v/v) aqueous-organic phase separation (see Fig. S9, Supplementary material and Fig. 7B). Surprisingly, the extraction efficiency increased dramatically from 53.9 ± 5.8% to 98.9 ± 3.1% when the phase separation-extraction process was repeated three times (Fig. 7B), indicating almost complete ATX recovery from the *H. pluvialis* cysts.

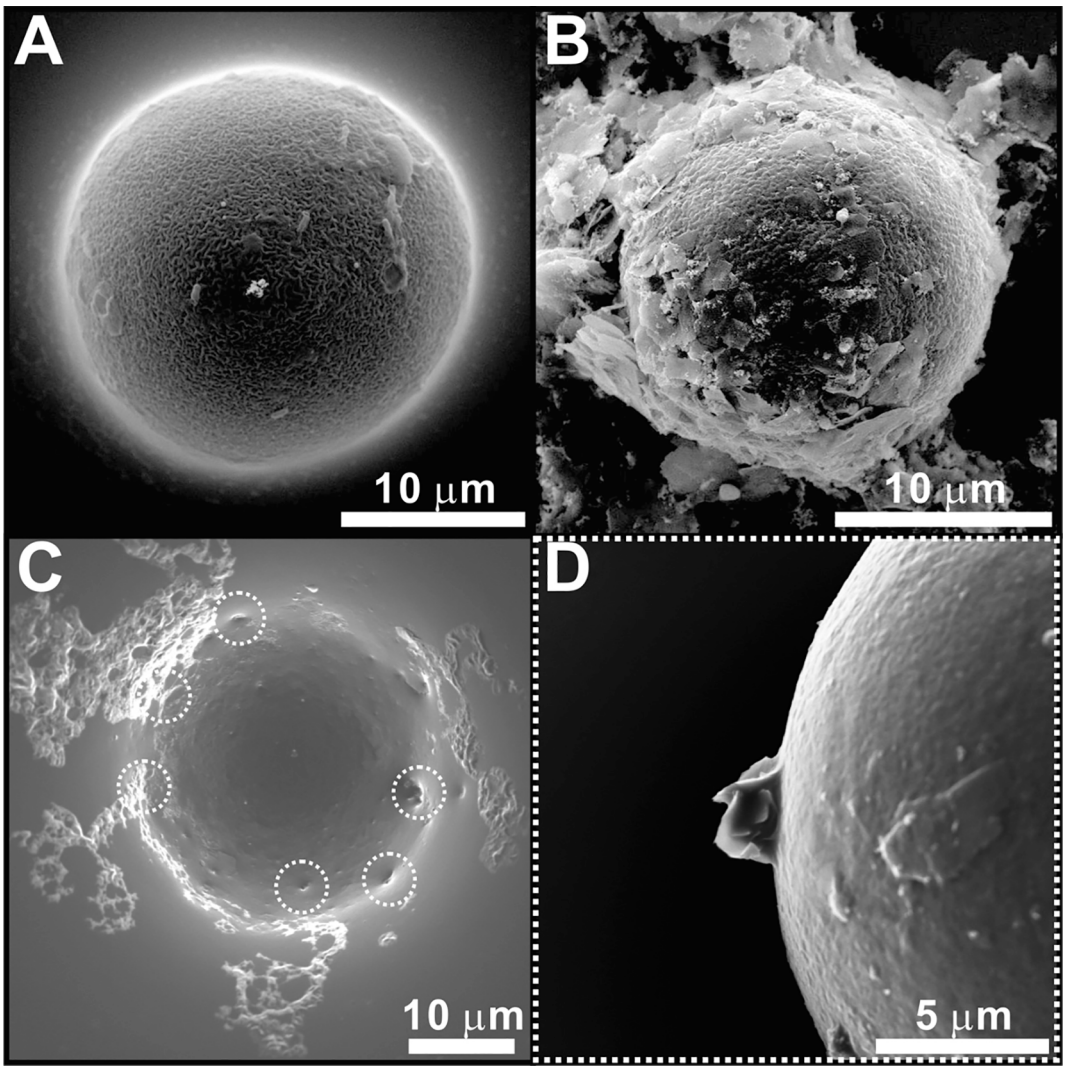

Fig. 6. *Ex situ* FESEM images of *H. pluvialis* cyst cells before (A) and after 5 min ultrasonication with α-quartz NPLs (B – D). (B) FESEM image showing the presence of α-quartz NPLs on the surface of a cell. (C) FESEM image showing whitish residues of ATX-containing lipids likely released from cell wall lesions generated by α-quartz NPLs during the extraction process (dotted white circles and refer to Fig. 5C^{+}). (D) Side-view FESEM image of one of the dotted white circles showing single α-quartz NPL embedded in a cell wall.

3.4. Discussions

3.4.1. Formation of two-dimensional α-quartz NPLs from the dissolution of ASNs under hydrothermal conditions

Several control experiments were performed to confirm the dissolution of ASNs by NaOH to assess the formation of α-quartz NPLs. First, no α-quartz NPLs were formed when the ASNs did not react with NaOH and were not partially neutralized with HCl under hydrothermal conditions. Second, almost no α-quartz NPLs formed when the ASNs were replaced with organosilicon-based precursors, such as TMOS, TEOS, and silane coupling reagent 3-aminopropyl triethoxysilane (APTES), which are typically used to synthesize and functionalize silica nanoparticles. Third, no α-quartz NPLs were produced when the NaOH to HCl molar ratio deviated from 3:1. These results suggest that an optimal amount of hydroxyl ions is needed to produce specific silicic precursor ions from ASNs. Moreover, these precursors are responsible for the nucleation and growth of α-quartz NPLs.

It is unclear why the dissolution of ASNs followed by the hydrothermal conditions leads to the formation of the anisotropic nanoplates rather than the isotropic nanoparticles of α-quartz in the absence of growth modifying additives. Only two possible mechanisms could result in the preferential two-dimensional anisotropic growth of crystals considering that typical crystals grow with a very thin plate- or sheet-like morphology despite belonging to a crystal class exhibiting a natural habit that is fairly uniform in dimensions along all three principal axes. One involves the selective poisoning of particular crystal faces by ions or surfactants, for example, which force the crystal to adapt a plate-like morphology [82,83]. The other involves the specific interface where the growth actually occurs, preventing growth from occurring perpendicular to the nanoplates faces [84–87]. This system did not contain any surfactant. Hence, the second mechanism is favored, suggesting that the liquid–vapor interface potentially formed in the autoclave reactor under these hydrothermal conditions could well have a very steep temperature or concentration gradient perpendicular to the interface. Moreover, these gradients would likely cause growth to occur in the plane of the interface.

3.4.2. α-Quartz NPLs assisted microalgal extraction

The ability of microalgal cells to resist rupture by mechanical stimuli was attributed to the mechanical strength and thickness of the cell walls [88,89]. Table S3 (Supplementary material) provides a comparison of the physical and compositional characteristics of four algal cell walls and associated biotechnological applications. Note that the thickness of the *H. pluvialis* cyst cell wall ranges from 1.8 to 2.2 μm and is

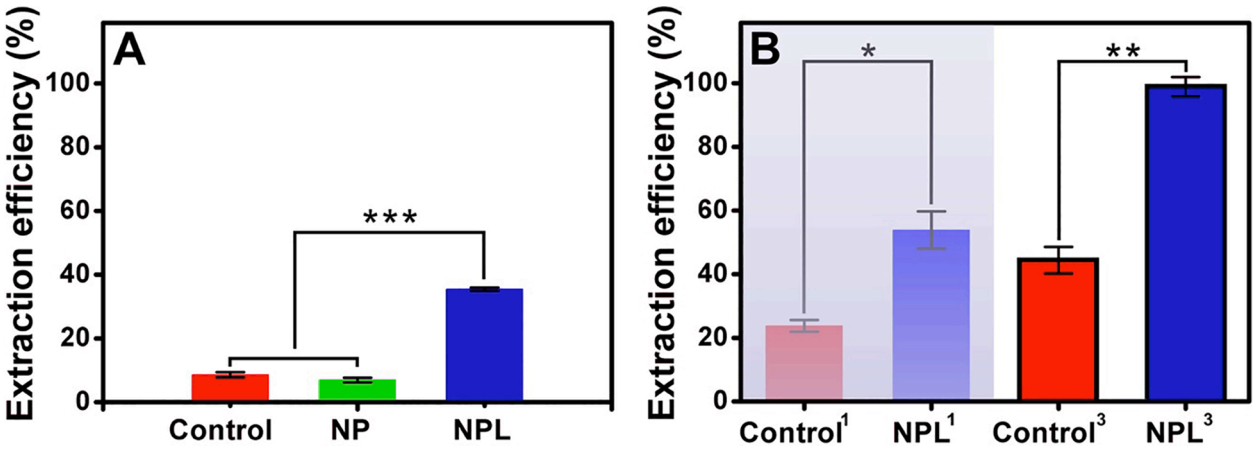

Fig. 7. Astaxanthin (ATX) extraction efficiencies, expressed as percentages of the amount of ATX extracted from *H. pluvialis* cyst cells, after α-quartz NPL treatment. (A) ATX extraction efficiencies were determined from a single 5 min ultrasonication cycle followed by extraction for 30 min by anhydrous DCM/MeOH (1:1, v/v) in the absence of neither ASNs nor α-quartz NPLs (Control, red bar), and in the presence of spherical ASNs (NP, green bar) or α-quartz NPLs (NPL, blue bar) at room temperature. (B) Comparison of (left) single and (right) multiple cycles of 5 min ultrasonication followed by 30 min DCM/MeOH/H_2O (1:1:2 (v/v)) extraction in the absence (Control^3, red bar) and the presence of α-quartz NPLs (NPL^3, blue bar). The superscripts indicate the numbers of cycles. The error bars represent the standard deviations of three independent experiments and the asterisks show the significances of differences (*, $P < 0.05$; **, $P < 0.005$; ***, and $P < 0.001$). (For interpretation of the references to color in this figure legend, the reader is referred to the web version of this article.)

significantly greater than the those of *Chlamydomonas* [90], *Chlorella* [89], and *Nannochloropsis* [89] (~351, ~88, and ~15 nm, respectively), which are used in widely different microalgae biorefinery purposes. Mature *H. pluvialis* cysts develop a highly robust, three-layered rigid cell wall and synthesize various secondary ketocarotenoid pigments, such as neoxanthin, lutein, canthaxanthin, zeaxanthin, and ATX, under favorable conditions during photosynthetic growth [91]. Fig. S7 (Supplementary material) shows HPLC chromatograms of the solvent extract of α-quartz NPLs-treated *H. pluvialis* biomass. The peaks were resolved adequately based on the information of carotenoid reference standards, suggesting that α-quartz NPL does not have any specificity for extracting certain types of carotenoid pigments. The cell walls consist of multiple layers of sporopollenin material (algaenan), nonhydrolyzable aliphatic biopolymers, proteins, cellulose, mannose, and carbohydrates [92]. The mass of the cell wall of the *H. pluvialis* cyst was reported to be approximately 15% of the total dry cell mass after three months of cultivation [81]. Therefore, the sturdy, complex structure of the *H. pluvialis* cyst cell wall provides excellent resistance to mechanical and chemical perturbations and constitutes the main barrier to the recovery of cell-manufactured intracellular lipids and bioactive chemicals, making the extraction of ATX quite challenging.

Understanding the mechanism of α-quartz NPLs-assisted cell wall disruption requires a consideration of the elastic modulus, i.e., the ability of the cell walls to resist and recover from deformation under the impact of mechanical forces. In one study, a large number of stiffness measurements for algal cells showed values ranging from 1 and 100 MPa, and the average values were ~1000 times softer than those of terrestrial plants [93]. The bulk elastic moduli (Young's moduli (E_C)) of living cells are directly proportional to the $\Delta P/(\Delta V/V)$ ratios (where ΔP is the change in cell turgor pressure and $\Delta V/V$ is the fractional change in cell volume). Applying this concept to a balloon and a soccer ball, the former has a low E_C and its shape changes considerably under small loads, whereas deformation of the latter requires large loads. Because the change in internal pressure (ΔP) for a given change in volume ($\Delta V/V$) is significantly smaller for a balloon than a soccer ball, a balloon model would appear to reflect the elastic properties of algal cells better because their cell walls are characterized by low stiffness and high extensibility [94]. Although a determination of the absolute E_C values of living cells is difficult, the force-distance curves obtained by atomic force microscopy (AFM) provided estimated E_C values of the algal cell walls between 0 and 25 MPa, as determined by Hertz contact mechanics [89,94–96]. Obataya et al. conducted force measurements on human epidermal melanocytes (E_C = 2–10 kPa) in a physiological medium using conventional or ultrathin nanoneedle AFM probes [97]. Their results suggested that the impact forces and indentation depths required for cell membrane penetration were much smaller when the nanoneedle used for measurements had a sharper tip (<~250 nm diameter) and a high geometric aspect ratio (~7 μm in length) than a conventional pyramidal tip with a low aspect ratio [97]. When the same logic is applied to α-quartz NPLs, their extremely narrower thickness (<~10 nm thickness) and high geometric aspect ratio (~1 μm in lateral size) will enable them to indent or penetrate cell membranes easily. Although it is unclear if their interactions with membranes under mild ultrasonic agitation provide sufficient collisional energy to rupture the membranes, ultrasonic treatment in the presence of α-quartz NPLs facilitated the efficient extraction of ATX.

These findings showing enhanced ATX recovery from *H. pluvialis* cysts by α-quartz NPLs/ultrasonication treatment before extraction raises the question as to why this process achieves much higher ATX extraction efficiencies than the extraction processes that do not use α-quartz NPLs. Organic solvents are detrimental to microalgal cells and cause them to shrink or swell and eventually cease functioning with non-natural conformations [98]. In H_2O, cells maintain their structural conformations, and solvent molecules can transit the cell membranes because of their enhanced permeability when subjected to phase separation-extraction processes [99]. These findings show that the extraction of intracellular entities is enhanced considerably when the cell walls are lacerated with α-quartz NPLs.

Two factors would be expected to boost the cell wall lesion density, i.e., α-quartz NPL concentration and biphasic separation. As the concentration increased, the extraction efficiency increased asymptotically to saturation (Fig. S8, Supplementary material). Biphasic separation, which occurred upon the addition of H_2O to DCM/MeOH, resulted in an upper aqueous layer containing H_2O, MeOH, α-quartz NPLs, and algal cells and a lower organic DCM layer containing the extracted ATX-rich lipids exclusively (see Fig. S13, Supplementary material). Owing to the intrinsic hydrophilicity of the cell walls of the *H. pluvialis* cysts and the hydroxyl-terminated surfaces of α-quartz NPLs, as indicated by the ^{29}Si ssNMR results, zeta-potential measurements, and the dispersion behavior of α-quartz NPLs in aqueous solution (Figs. S1, S11, and S12, Supplementary material, respectively), the interaction between the cells and NPLs was sufficient to trap them on the cell walls (see Fig. 6B).

Based on the dielectric constants (ε) of H_2O, MeOH, and DCM at 25 °C, which are 80.1, 32.7, and 8.93, respectively, the overall ε of the DCM/MeOH/H_2O mixture increased with increasing proportion of H_2O. This increase, which is an ε value approximately three times than that of anhydrous DCM/MeOH, is likely to reduce the attractive affinity between the cells and NPLs and enable them to separate and disperse in an aqueous layer. Redispersing and ultrasonicating the algal cell-α-quartz NPLs precipitates in an aqueous solution will allow the NPLs to increase the rate of Brownian motion promoted by the turbulence of solvent flow and circulating eddies [100]. The resulting increase in NPL dynamic motion will boost the collision rate of NPLs on the cell membranes while preventing NPLs from adhering to the cell walls. Therefore, the repeated dispersion and ultrasonication steps of phase separation-extraction processes can increase not only cell wall lesion densities but also the ATX extraction and recovery efficiencies from cells with an almost normal cellular morphology.

4. Conclusions

This paper reported a template-free, solution-phase synthesis of two-dimensional ultrathin α-quartz NPLs, 1–2 μm in lateral size and 7–8 nm in thickness, under relatively mild hydrothermal conditions (250 °C and autogenic pressure) in the absence of any growth modifiers or additives in ~4 h. The structure and composition of the α-quartz NPLs were characterized using a battery of analytical techniques. The as-synthesized NPLs exhibited highly crystalline lattice structures that closely matched that of α-quartz with excellent thermal and pH stability. In addition, α-quartz NPLs were harnessed to recover ATX from microalgal *H. pluvialis* cells with a sturdy cell wall. ATX was secured from *H. pluvialis* by < 5 min facile ultrasonication followed by multiple phase separation-extraction processes with an extraction efficiency of ~99% (18.0 ± 0.6 mg ATX/g cell). The amount of anisotropic α-quartz NPL dosing for the maximum ATX extraction was determined to be 800.0 mg/L, which was substantially lower than the routine dosages of isotropic nanomaterials for extraction controls. The enhanced extraction efficiency and dosage were attributed to the characteristic anisotropic structure of ultrathin α-quartz NPL that expedited the formation of cell wall lesions.

The findings of the present study are meaningful in two regards. First, they provide a facile, scalable, and cost-effective means of producing novel α-quartz nanoplates of high crystal quality and relatively narrow size distribution using template-free, mild hydrothermal reactions, potentially offering new materials for manufacturing, engineering, optoelectronic, energy storage, pharmaceutical, and biomedical applications. Second, they reveal the previously overlooked importance of an anisotropic ultrathin plate-like nanostructure that endows quartz with superior cell wall disruption activity in the microalgal extraction processes under relatively moderate conditions. Typical biorefinery processes involving microalgal systems prefer mechanical over chemical or biological methods that ultimately destroy the microalgae regardless of the species or biomass conditions. Furthermore, these mechanical processes require high-energy inputs to generate high shearing forces under abrupt pressure gradients, high turbulence, and excessive hydrodynamic cavitation. Therefore, they are unsuitable for the recovery of intracellular ATX, which is quite sensitive to physical and chemical environments under harsh conditions leading to oxidation and thermal degradation [50,51,101]. The use of α-quartz NPLs, ultrasonic agitation, and biphasic extraction for ATX harvesting not only provide a *potential* means of mitigating the risks of degradation of bioactive ATX, but offers a functional nanomaterial-based engineering approach to the efficient, low cost, large-scale extraction of other valuable algal products from sustainable algal harvesting biorefinery operations. Understanding the mechanism responsible for the formation of ultrathin α-quartz NPLs and their role in the extraction of ATX from *H. pluvialis* would undoubtedly represent significant progress toward the design of highly efficient microalgal biorefinery processes.

5. Data availability

The data that support the findings of this study are available from the corresponding authors upon reasonable request.

Declaration of Competing Interest

The authors declare that they have no known competing financial interests or personal relationships that could have influenced the work reported in this paper.

Acknowledgements

This work was supported by the Basic Science Research Program through the National Research Foundation of Korea (NRF) funded by the Ministry of Education of Korea (NRF-2019R1F1A1060060), the National Research Foundation of Korea (NRF) funded by the Ministry of Science and ICT, Republic of Korea (NRF-2019R1A2C1003463), the Research/Development Program of the Korea Institute of Energy Research (KIER-C0-2424), Nano-Material Technology Development Program through the National Research Foundation of Korea (NRF) funded by the Ministry of Science, ICT and Future Planning (2009-0082580), and the National Research Foundation of Korea (NRF) funded by the Korean government (MSIT) (NRF-2017R1A5A1015365).

Appendix A. Supplementary data

Supplementary data to this article can be found online at https://doi.org/10.1016/j.cej.2020.127467.

References

[1] B. Mason, L.G. Berry, Elements of mineralogy, W. H. Freeman, San Francisco, 1968.
[2] C.H. Yoder, Appendix 4: Quartz, Ionic Compounds: Applications of Chemistry to Mineralogy, Wiley (2006) 173–175.
[3] D.R. Spearing, I. Farnan, J.F. Stebbins, Dynamics of the alpha-beta phase-transitions in quartz and cristobalite as observed by in-situ high-temperature ^{29}Si NMR and ^{17}O NMR, Phys. Chem. Miner. 19 (1992) 307–321.
[4] C.S. Brown, R.C. Kell, L.A. Thomas, N. Wooster, W.A. Wooster, The growth and properties of large crystals of synthetic quartz, Mineral. Mag. J. Mineral. Soc. 29 (217) (1952) 858–874.
[5] P. Saha, N. Annamalai, A.K. Guha, Synthetic Quartz Production and Applications, Trans. Indian Ceram. Soc. 50 (5) (1991) 129–135.
[6] N. Wooster, W.A. Wooster, Preparation of synthetic quartz, Nature 157 (1946) 297-297.
[7] T. Coradin, P.J. Lopez, Biogenic silica patterning: simple chemistry or subtle biology? ChemBioChem 4 (4) (2003) 251–259.
[8] T. Coradin, P.J. Lopez, C. Gautier, J. Livage, From biogenic to biomimetic silica, C.R. Palevol 3 (6-7) (2004) 443–452.
[9] P.J. Lopez, C. Gautier, J. Livage, T. Coradin, Mimicking biogenic silica nanostructures formation, Curr. Nanosci. 1 (2005) 73–83.
[10] S.V. Patwardhan, Biomimetic and bioinspired silica: recent developments and applications, Chem. Commun. 47 (2011) 7567–7582.
[11] C.M. Zaremba, G.D. Stucky, Biosilicates and biomimetic silicate synthesis, Curr. Opin. Solid State Mater. Sci. 1 (3) (1996) 425–429.
[12] L.G. Benning, V.R. Phoenix, N. Yee, K.O. Konhauser, The dynamics of cyanobacterial silicification: an infrared micro-spectroscopic investigation, Geochim. Cosmochim. Acta 68 (4) (2004) 743–757.
[13] N. Kröger, N. Poulsen, Diatoms-from cell wall biogenesis to nanotechnology, Annu. Rev. Genet. 42 (1) (2008) 83–107.
[14] F. Westall, L. Boni, E. Guerzoni, The experimental silicification of microorganisms, Palaeontology 38 (1995) 495–528.
[15] C. Levi, J.L. Barton, C. Guillemet, E. Le Bras, P. Lehuede, A remarkably strong natural glassy rod: the anchoring spicule of theMonorhaphis sponge, J. Mater. Sci. Lett. 8 (3) (1989) 337–339.
[16] H. Lowenstam, Minerals formed by organisms, Science 211 (4487) (1981) 1126–1131.
[17] S. Mann, Molecular tectonics in biomineralization and biomimetic materials chemistry, Nature 365 (6446) (1993) 499–505.
[18] S. Mann, G.A. Ozin, Synthesis of inorganic materials with complex form, Nature 382 (6589) (1996) 313–318.
[19] S. Oliver, A. Kuperman, N. Coombs, A. Lough, G.A. Ozin, Lamellar aluminophosphates with surface patterns that mimic diatom and radiolarian microskeletons, Nature 378 (6552) (1995) 47–50.

[20] E.D.E.R. Hyde, A. Seyfaee, F. Neville, R. Moreno-Atanasio, Colloidal Silica Particle Synthesis and Future Industrial Manufacturing Pathways: A Review, Ind. Eng. Chem. Res. 55 (33) (2016) 8891–8913.
[21] G. Qiao, L. Liu, X. Hao, J. Zheng, W. Liu, J. Gao, C.C. Zhang, Q. Wang, Signal transduction from small particles: sulfur nanodots featuring mercury sensing, cell entry mechanism and in vitro tracking performance, Chem. Eng. J. 382 (2020), 122907.
[22] Z. Zhou, Y. Zheng, J. Gao, L. Jiang, Q. Wang, Two novel sol–gel-derived nanostructures and their hemoglobin sensing features, J Sol-Gel Sci Technol 77 (1) (2016) 205–210, https://doi.org/10.1007/s10971-015-3845-7.
[23] P. Bettermann, F. Liebau, Transformation of amorphous silica to crystalline silica under hydrothermal conditions, Contrib. Mineral Petrol. 53 (1975) 25–36.
[24] W.S. Fyfe, D.S. McKay, Hydroxyl ion catalysis of the crystallization of amorphous silica at 330 °C and some observations on the hydrolysis of albite solutions, Am. Mineral. 47 (1962) 83–89.
[25] Y.-H. Jung, S.P. Pack, S. Chung, Solvothermal synthesis and characterization of highly monodisperse organically functionalized vanadium oxide nanocrystals for thermochromic applications, Mater. Res. Bull. 101 (2018) 67–72, https://doi.org/10.1016/j.materresbull.2018.01.014.
[26] J. Liu, L.u. Wang, J. Wang, L. Zhang, Simple solvothermal synthesis of hydrophobic magnetic monodispersed Fe_3O_4 nanoparticles, Mater. Res. Bull. 48 (2) (2013) 416–421, https://doi.org/10.1016/j.materresbull.2012.10.060.
[27] X. Wang, J. Zhuang, Q. Peng, Y. Li, A general strategy for nanocrystal synthesis, Nature 437 (7055) (2005) 121–124, https://doi.org/10.1038/nature03968.
[28] M. Yoshimura, K. Byrappa, Hydrothermal processing of materials: past, present and future, J. Mater. Sci. 43 (2008) 2085–2103.
[29] J.F. Bertone, J. Cizeron, R.K. Wahi, J.K. Bosworth, V.L. Colvin, Hydrothermal Synthesis of Quartz Nanocrystals, Nano Lett. 3 (5) (2003) 655–659, https://doi.org/10.1021/nl025854r.
[30] X. Jiang, Y.-B. Jiang, C.J. Brinker, Hydrothermal synthesis of monodisperse single-crystalline alpha-quartz nanospheres, Chem. Commun. 47 (26) (2011) 7524, https://doi.org/10.1039/c1cc11115a.
[31] L.M. Sochalski-Kolbus, H.-W. Wang, A.J. Rondinone, L.M. Anovitz, D. J. Wesolowski, P.S. Whitfield, Solvothermal Synthesis and Surface Chemistry To Control the Size and Morphology of Nanoquartz, Cryst. Growth Des. 15 (11) (2015) 5327–5331, https://doi.org/10.1021/acs.cgd.5b00882.
[32] P. Buckley, N. Hargreaves, S. Cooper, Nucleation of quartz under ambient conditions, Commun Chem 1 (1) (2018), https://doi.org/10.1038/s42004-018-0049-4.
[33] C. Büchner, M. Heyde, Two-dimensional silica opens new perspectives, Prog. Surf. Sci. 92 (4) (2017) 341–374, https://doi.org/10.1016/j.progsurf.2017.09.001.
[34] Y. Xue, Y.-S. Ye, F.-Y. Chen, H. Wang, C. Chen, Z.-G. Xue, X.-P. Zhou, X.-L. Xie, Y.-W. Mai, A simple and controllable graphene-templated approach to synthesise 2D silica-based nanomaterials using water-in-oil microemulsions, Chem. Commun. 52 (3) (2016) 575–578, https://doi.org/10.1039/C5CC06941F.
[35] X. Xiang, J.Y. Wu, Q.X. Shi, Q. Xia, Z.G. Xue, X.L. Xie, Y.S. Ye, Mesoporous silica nanoplates facilitating fast Li + diffusion as effective polysulfide-trapping materials for lithium–sulfur batteries, J. Mater. Chem. A 7 (15) (2019) 9110–9119, https://doi.org/10.1039/C8TA11446C.
[36] M.M. Tomczak, D.D. Glawe, L.F. Drummy, C.G. Lawrence, M.O. Stone, C.C. Perry, D.J. Pochan, T.J. Deming, R.R. Naik, Polypeptide-Templated Synthesis of Hexagonal Silica Platelets, J. Am. Chem. Soc. 127 (36) (2005) 12577–12582, https://doi.org/10.1021/ja0524503.s001.
[37] S.V. Patwardhan, R. Maheshwari, N. Mukherjee, K.L. Kiick, S.J. Clarson, Conformation and assembly of polypeptide scaffolds in templating the synthesis of silica: An example of a polylysine macromolecular "switch", Biomacromolecules 7 (2006) 491–497.
[38] H. Chen, L. Xia, W. Fu, Z. Yang, Z. Li, One-step synthesis of water dispersible silica nanoplates, Chem. Commun. 49 (13) (2013) 1300, https://doi.org/10.1039/c2cc38293h.
[39] B. Singh, V. Polshettiwar, Solution-phase synthesis of two-dimensional silica nanosheets using soft templates and their applications in CO 2 capture, Nanoscale 11 (12) (2019) 5365–5376, https://doi.org/10.1039/C8NR10119A.
[40] H. Chen, W. Fu, Z. Li, Temperature and pH Responsive Janus Silica Nanoplates Prepared by the Sol–Gel Process and Postmodification, Langmuir 36 (1) (2020) 273–278, https://doi.org/10.1021/acs.langmuir.9b03396.s001.
[41] P.M. Foley, E.S. Beach, J.B. Zimmerman, Algae as a source of renewable chemicals: opportunities and challenges, Green Chem. 13 (6) (2011) 1399, https://doi.org/10.1039/c1gc00015b.
[42] D.R. Georgianna, S.P. Mayfield, Exploiting diversity and synthetic biology for the production of algal biofuels, Nature 488 (7411) (2012) 329–335, https://doi.org/10.1038/nature11479.
[43] T.M. Mata, A.A. Martins, N.S. Caetano, Microalgae for biodiesel production and other applications: A review, Renew. Sustain. Energy Rev. 14 (1) (2010) 217–232, https://doi.org/10.1016/j.rser.2009.07.020.
[44] Y.-K. Oh, K.-R. Hwang, C. Kim, J.R. Kim, J.-S. Lee, Recent developments and key barriers to advanced biofuels: A short review, Bioresour. Technol. 257 (2018) 320–333, https://doi.org/10.1016/j.biortech.2018.02.089.
[45] R. Praveenkumar, K. Lee, J. Lee, Y.K. Oh, Breaking dormancy: An energy-efficient means of recovering astaxanthin from microalgae, Green Chem. 17 (2015) 1226–1234.
[46] O. Pulz, W. Gross, Valuable products from biotechnology of microalgae, Appl Microbiol Biotechnol 65 (6) (2004) 635–648, https://doi.org/10.1007/s00253-004-1647-x.
[47] G.S. di Visconte, A. Spicer, C.J. Chuck, M.J. Allen, The microalgae biorefinery: A Perspective on the Current Status and Future Opportunities Using Genetic Modification, Appl. Sci. 9 (2019).
[48] J.A. Posada, L.B. Brentner, A. Ramirez, M.K. Patel, Conceptual design of sustainable integrated microalgae biorefineries: Parametric analysis of energy use, greenhouse gas emissions and techno-economics, Algal Res. 17 (2016) 113–131.
[49] R. Praveenkumar, R. Gwak, M. Kang, T.S. Shim, S. Cho, J. Lee, Y.-K. Oh, K. Lee, B. Kim, Regenerative Astaxanthin Extraction from a Single Microalgal (Haematococcus pluvialis) Cell Using a Gold Nano-Scalpel, ACS Appl. Mater. Interfaces 7 (40) (2015) 22702–22708, https://doi.org/10.1021/acsami.5b07651.
[50] D.-Y. Kim, D. Vijayan, R. Praveenkumar, J.-I. Han, K. Lee, J.-Y. Park, W.-S. Chang, J.-S. Lee, Y.-K. Oh, Cell-wall disruption and lipid/astaxanthin extraction from microalgae: Chlorella and Haematococcus, Bioresour. Technol. 199 (2016) 300–310, https://doi.org/10.1016/j.biortech.2015.08.107.
[51] S.Y. Lee, J.M. Cho, Y.K. Chang, Y.-K. Oh, Cell disruption and lipid extraction for microalgal biorefineries: A review, Bioresour. Technol. 244 (2017) 1317–1328, https://doi.org/10.1016/j.biortech.2017.06.038.
[52] S.-A. Choi, Y.-K. Oh, J. Lee, S.J. Sim, M.E. Hong, J.-Y. Park, M.-S. Kim, S.W. Kim, J.-S. Lee, High-efficiency cell disruption and astaxanthin recovery from Haematococcus pluvialis cyst cells using room-temperature imidazolium-based ionic liquid/water mixtures, Bioresour. Technol. 274 (2019) 120–126, https://doi.org/10.1016/j.biortech.2018.11.082.
[53] Y.-C. Lee, K. Lee, Y.-K. Oh, Recent nanoparticle engineering advances in microalgal cultivation and harvesting processes of biodiesel production: A review, Bioresour. Technol. 184 (2015) 63–72, https://doi.org/10.1016/j.biortech.2014.10.145.
[54] M.K. Nguyen, J.-Y. Moon, V.K.H. Bui, Y.-K. Oh, Y.-C. Lee, Recent advanced applications of nanomaterials in microalgae biorefinery, Algal Res. 41 (2019), 101522.
[55] S. Abdul Razack, S. Duraiarasan, V. Mani, Biosynthesis of silver nanoparticle and its application in cell wall disruption to release carbohydrate and lipid from C. vulgaris for biofuel production, Biotechnol. Rep, 11 (2016) 70–76, https://doi.org/10.1016/j.btre.2016.07.001.
[56] W.-C. Huang, J.-D. Kim, Nickel oxide nanoparticle-based method for simultaneous harvesting and disruption of microalgal cells, Bioresour. Technol. 218 (2016) 1290–1293, https://doi.org/10.1016/j.biortech.2016.07.091.
[57] J.Y. Seo, R. Praveenkumar, B. Kim, J.-C. Seo, J.-Y. Park, J.-G. Na, S.G. Jeon, S. B. Park, K. Lee, Y.-K. Oh, Downstream integration of microalgae harvesting and cell disruption by means of cationic surfactant-decorated Fe 3 O 4 nanoparticles, Green Chem. 18 (14) (2016) 3981–3989, https://doi.org/10.1039/C6GC00904B.
[58] Y.-C. Lee, Y.S. Huh, W. Farooq, J. Chung, J.-I. Han, H.-J. Shin, S.H. Jeong, J.-S. Lee, Y.-K. Oh, J.-Y. Park, Lipid extractions from docosahexaenoic acid (DHA)-rich and oleaginous Chlorella sp. biomasses by organic-nanoclays, Bioresour. Technol. 137 (2013) 74–81, https://doi.org/10.1016/j.biortech.2013.03.090.
[59] S.-H. Kim, Y. Huang, C. Sawatdeenarunat, S. Sung, V.-Y. Lin, Selective sequestration of carboxylic acids from biomass fermentation by surface-functionalized mesoporous silica nanoparticles, J. Mater. Chem. 21 (32) (2011) 12103, https://doi.org/10.1039/c1jm11299f.
[60] J.S. Valenstein, K. Kandel, F. Melcher, I.I. Slowing, V.-Y. Lin, B.G. Trewyn, Functional Mesoporous Silica Nanoparticles for the Selective Sequestration of Free Fatty Acids from Microalgal Oil, ACS Appl. Mater. Interfaces 4 (2) (2012) 1003–1009, https://doi.org/10.1021/am201647t.
[61] S.-A. Choi, Y. Jeong, J. Lee, Y.H. Huh, S.H. Choi, H.-S. Kim, D.-H. Cho, J.-S. Lee, H. Kim, H.-R. An, S. Lee, E.C. Park, S.W. Kim, K.-R. Hwang, E. Moon, Y.-K. Oh, H. U. Lee, Biocompatible liquid-type carbon nanodots (C-paints) as light delivery materials for cell growth and astaxanthin induction of Haematococcus pluvialis, Mater. Sci. Eng., C 109 (2020) 110500, https://doi.org/10.1016/j.msec.2019.110500.
[62] W. Stöber, A. Fink, E. Bohn, Controlled growth of monodisperse silica spheres in the micron size range, J. Colloid Interface Sci. 26 (1) (1968) 62–69, https://doi.org/10.1016/0021-9797(68)90272-5.
[63] E.H. Jang, S.P. Pack, I. Kim, S. Chung, A systematic study of hexavalent chromium adsorption and removal from aqueous environments using chemically functionalized amorphous and mesoporous silica nanoparticles, Sci. Rep. 10 (2020) 5558.
[64] K. Momma, F. Izumi, VESTA: a three-dimensional visualization system for electronic and structural analysis, J. Appl. Crystallogr. 41 (2008) 653–658.
[65] Y.Y. Choi, M.E. Hong, E.S. Jin, H.M. Woo, S.J. Sim, Improvement in modular scalability of polymeric thin-film photobioreactor for autotrophic culturing of Haematococcus pluvialis using industrial flue gas, Bioresour. Technol. 249 (2018) 519–526, https://doi.org/10.1016/j.biortech.2017.10.060.
[66] M. Takeuchi, G. Martra, S. Coluccia, M. Anpo, Evaluation of the Adsorption States of H 2 O on Oxide Surfaces by Vibrational Absorption: Near- and Mid-Infrared Spectroscopy, J. Near Infrared Spectrosc. 17 (6) (2009) 373–384, https://doi.org/10.1255/jnirs.843.
[67] B.-G. Kim, S.-Y. Kang, J.-J. Kim, FTIR study of fluorinated silicon oxide film, Journal of Physics D: Appl. Phys. 30 (1997) 1720–1724.
[68] C.T. Kirk, Quantitative analysis of the effect of disorder-induced mode coupling on infrared absorption in silica, Phys. Rev. B 38 (2) (1988) 1255–1273, https://doi.org/10.1103/PhysRevB.38.1255.
[69] M.C. Matos, L.M. Ilharco, R.M. Almeida, The evolution of TEOS to silica gel and glass by vibrational spectroscopy, J. Non-Cryst. Solids 147-148 (1992) 232–237, https://doi.org/10.1016/S0022-3093(05)80622-2.

[70] S. Chen, A. Osaka, S. Hayakawa, K. Tsuru, E. Fujii, K. Kawabata, Microstructure evolution in Stöber-type silica nanoparticles and their in vitro apatite deposition, J. Sol-Gel Sci. Technol. 48 (2008) 322–335.
[71] J.F. Scott, S.P.S. Porto, Longitudinal and Transverse Optical Lattice Vibrations in Quartz, Phys. Rev. 161 (3) (1967) 903–910, https://doi.org/10.1103/PhysRev.161.903.
[72] R.J. Hemley, Pressure dependence of Raman spectra of SiO2 polymorphs: α-quartz, coesite, and stishovite, High-Pressure Research in Mineral Physics: A Volume in Honor of Syun-Iti Akimoto (1987) 347-359.
[73] L.i. Wang, W. Sun, Y.-H. Hu, L.-H. Xu, Adsorption mechanism of mixed anionic/cationic collectors in Muscovite – Quartz flotation system, Miner. Eng. 64 (2014) 44–50, https://doi.org/10.1016/j.mineng.2014.03.021.
[74] R. Bywalez, H. Karacuban, H. Nienhaus, C. Schulz, H. Wiggers, Stabilization of mid-sized silicon nanoparticles by functionalization with acrylic acid, Nanoscale Res Lett 7 (1) (2012), https://doi.org/10.1186/1556-276X-7-76.
[75] J. Lee, J.H. Kim, K. Choi, H.G. Kim, J.A. Park, S.H. Cho, S.W. Hong, J.H. Lee, J. H. Lee, S. Lee, S.Y. Lee, J.W. Choi, Investigation of the mechanism of chromium removal in (3-aminopropyl)trimethoxysilane functionalized mesoporous silica, Sci. Rep. 8 (2018) 12078.
[76] N. Fellenz, F.J. Perez-Alonso, P.P. Martin, J.L. García-Fierro, J.F. Bengoa, S. G. Marchetti, S. Rojas, Chromium (VI) removal from water by means of adsorption-reduction at the surface of amino-functionalized MCM-41 sorbents, Microporous Mesoporous Mater. 239 (2017) 138–146, https://doi.org/10.1016/j.micromeso.2016.10.012.
[77] X. Lv, L. Zhang, F. Xing, H. Lin, Controlled synthesis of monodispersed mesoporous silica nanoparticles: Particle size tuning and formation mechanism investigation, Micropor. Mesopor. Mat. 225 (2016) 238–244.
[78] G.S. Smith, L.E. Alexander, Refinement of the atomic parameters of alpha-quartz, Acta Crystallogr. 16 (1963) 462–471.
[79] P.-H. Wei, The structure of alpha-quartz, Z. Kristallogr. 92 (1935) 355–362.
[80] F. Li, M. Cai, M. Lin, X. Huang, J. Wang, X. Zheng, S. Wu, Y.u. An, Accumulation of Astaxanthin Was Improved by the Nonmotile Cells of Haematococcus pluvialis, Biomed Res. Int. 2019 (2019) 1–7, https://doi.org/10.1155/2019/8101762.
[81] C. Hagen, S. Siegmund, W. Braune, Ultrastructural and chemical changes in the cell wall of Haematococcus pluvialis (Volvocales, Chlorophyta) during aplanospore formation, Eur. J. Phycol. 37 (2002) 217-226.
[82] S.R. Qiu, A. Wierzbicki, E.A. Salter, S. Zepeda, C.A. Orme, J.R. Hoyer, G. H. Nancollas, A.M. Cody, J.J. De Yoreo, Modulation of Calcium Oxalate Monohydrate Crystallization by Citrate through Selective Binding to Atomic Steps, J. Am. Chem. Soc. 127 (25) (2005) 9036–9044, https://doi.org/10.1021/ja043591s.
[83] M.L. Weaver, S.R. Qiu, J.R. Hoyer, W.H. Casey, G.H. Nancollas, J.J. De Yoreo, Inhibition of calcium oxalate monohydrate growth by citrate and the effect of the background electrolyte, J. Cryst. Growth 306 (1) (2007) 135–145, https://doi.org/10.1016/j.jcrysgro.2007.04.053.
[84] S.A. McCarthy, R. Ratkic, F. Purcell-Milton, T.S. Perova, Y.K. Gun'ko, Adaptable surfactant-mediated method for the preparation of anisotropic metal chalcogenide nanomaterials, Sci Rep 8 (1) (2018), https://doi.org/10.1038/s41598-018-21328-7.
[85] Z. Wu, S. Yang, W. Wu, Shape control of inorganic nanoparticles from solution, Nanoscale 8 (3) (2016) 1237–1259, https://doi.org/10.1039/C5NR07681A.
[86] J. Xiao, L. Qi, Surfactant-assisted, shape-controlled synthesis of gold nanocrystals, Nanoscale 3 (4) (2011) 1383, https://doi.org/10.1039/c0nr00814a.
[87] Q. Zhang, Y. Hu, S. Guo, J. Goebl, Y. Yin, Seeded Growth of Uniform Ag Nanoplates with High Aspect Ratio and Widely Tunable Surface Plasmon Bands, Nano Lett. 10 (12) (2010) 5037–5042, https://doi.org/10.1021/nl1032233.
[88] A.P.J. Middelberg, Process-scale disruption of microorganisms, Biotechnol. Adv. 13 (3) (1995) 491–551, https://doi.org/10.1016/0734-9750(95)02007-P.
[89] B.H.J. Yap, S.A. Crawford, R.R. Dagastine, P.J. Scales, G.J.O. Martin, Nitrogen deprivation of microalgae: effect on cell size, cell wall thickness, cell strength, and resistance to mechanical disruption, J. Ind. Microbiol. Biotechnol. 43 (2016) 1671–1680.
[90] G.-S. Ha, M.M. El-Dalatony, D.-H. Kim, E.-S. Salama, M.B. Kurade, H.-S. Roh, A. El-Fatah Abomohra, B.-H. Jeon, Biocomponent-based microalgal transformations into biofuels during the pretreatment and fermentation process, Bioresour. Technol. 302 (2020) 122809, https://doi.org/10.1016/j.biortech.2020.122809.
[91] Y.-E. Kim, I.A. Matter, N. Lee, M. Jung, Y.-C. Lee, S.-A. Choi, S.Y. Lee, J.R. Kim, Y.-K. Oh, Enhancement of astaxanthin production by Haematococcus pluvialis using magnesium aminoclay nanoparticles, Bioresour. Technol. 307 (2020), 123270.
[92] M.M.R. Shah, Y. Liang, J.J. Cheng, M. Daroch, Astaxanthin-producing green microalga Haematococcus pluvialis: From single cell to high value commercial products, Frontiers in Plant Sci. 7 (2016).
[93] M. Denny, B. Gaylord, The mechanics of wave-swept algae, J. Exp. Biol. 205 (2002) 1355–1362.
[94] B. Tesson, B. Charrier, Brown algal rnorphogenesis: atomic force microscopy as a tool to study the role of mechanical forces, Front. Plant Sci. 5 (2014).
[95] F. Jia, M. Ben Amar, B. Billoud, B. Charrier, Morphoelasticity in the development of brown alga Ectocarpus siliculosus : from cell rounding to branching, J. R. Soc. Interface: 14 (127) (2017) 20160596, https://doi.org/10.1098/rsif.2016.0596.
[96] M. Lekka, Discrimination Between Normal and Cancerous Cells Using AFM, BioNanoSci. 6 (1) (2016) 65–80.
[97] I. Obataya, C. Nakamura, Han, N. Nakamura, J. Miyake, Nanoscale Operation of a Living Cell Using an Atomic Force Microscope with a Nanoneedle, Nano Lett. 5 (1) (2005) 27–30.
[98] H.J. Heipieper, F.J. Weber, J. Sikkema, H. Keweloh, J.A.M. de Bont, Mechanisms of resistance of whole cells to toxic organic solvents, Trends Biotechnol. 12 (10) (1994) 409–415.
[99] X. Ren, X. Zhao, F. Turcotte, J.S. Deschênes, R. Tremblay, M. Jolicoeur, Current lipid extraction methods are significantly enhanced adding a water treatment step in Chlorella prototheocoides, Microb. Cell Fact. 16 (2017) 1–13.
[100] S.R. Shirsath, S.H. Sonawane, P.R. Gogate, Intensification of extraction of natural products using ultrasonic irradiations—A review of current status, Chem. Eng. Process. Process Intensif. 53 (2012) 10–23.
[101] M. Irshad, A.A. Myint, M.E. Hong, J. Kim, S.J. Sim, One-Pot, simultaneous cell wall disruption and complete extraction of astaxanthin from *H. pluvialis* at room temperature, ACS Sustainable Chem. Eng. 7 (16) (2019) 13898–13910.